Graphical Abstract

Two types of ridging South Atlantic Ocean anticyclones over South Africa and the associated dynamical processes

Thando Ndarana, Tsholanang S. Rammopo, Chris J. C. Reason, Mary-Jane Bopape, Francois Engelbrecht, Hector Chikoore

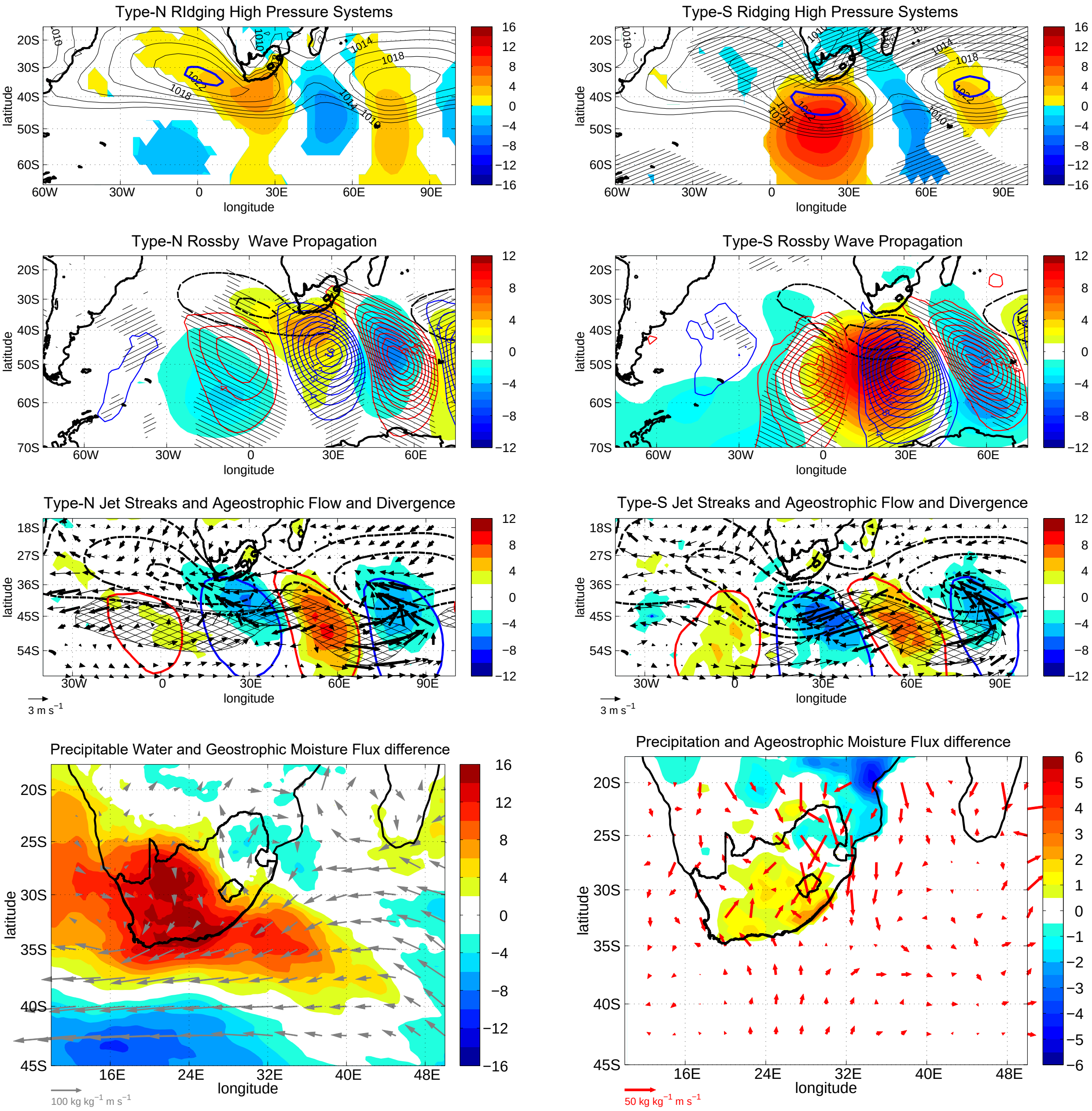

Highlights

Two types of ridging South Atlantic Ocean anticyclones over South Africa and the associated dynamical processes

Thando Ndarana, Tsholanang S. Rammopo, Chris J. C. Reason, Mary-Jane Bopape, Francois Engelbrecht, Hector Chikoore

- The study has shown that there are at least two types of ridging South Atlantic Ocean high pressure systems that affect South Africa; those that occur north of 40°S, called Type-N, and those that occur south of this latitude line, called Type-S.
- The two types of ridging are preceded and modulated by differently configured Rossby wave packets that propagate across the South Atlantic Ocean and mature as they pass South Africa, as the ridging process is initiated.
- Type-N ridging is associated with a double jet streak structure, whereas Type-S ridging has one downstream jet during the summer and a smaller scale upstream jet develops duing the colder month of the year.
- The onshore ageostrophic moisture fluxes associated with Type-S are stronger, leading to higher precipitation amounts than Type-N.

Two types of ridging South Atlantic Ocean anticyclones over South Africa and the associated dynamical processes

Thando Ndarana[a,*], Tsholanang S. Rammopo[a], Chris J. C. Reason[b], Mary-Jane Bopape[c], Francois Engelbrecht[d], Hector Chikoore[e]

[a] *Department of Geography, Geoinformatics and Meteorology, University of Pretoria, Hatfield, South Africa*
[b] *Department of Oceanography, University of Cape Town, Cape Town, South Africa*
[c] *Department of Research and Innovation, South African Weather Service, Centurion, South Africa*
[d] *Global Change Institute, University of the Witwatersrand, Johannesburg, South Africa*
[e] *Unit for Environmental Sciences and Management, North-West University, Vanderbijlpark, South Africa*

Abstract

Using 41 years of ERA5 reanalysis, two types of ridging South Atlantic Ocean high pressure systems were identified in the South African domain. Type-N events have a zonal structure and the ridging component breaks off from the parent South Atlantic Ocean anticyclone, after extending across the South African mainland. Type-S events extend south of the mainland and then break off. The Type-N (Type-S) ridging component is weaker (stronger) leaving behind a stronger (weaker) South Atlantic Ocean high. The two types of ridging events are associated with different configurations of Rossby wave packets that propagate across the South Atlantic Ocean. The surface and upper tropospheric anomalies associated with Type-S wave packets are stronger than those associated with Type-N events and the vertical coupling of the anomalies is much stringer during Type-S events. Type-N events are associated with a double jet streak structure, with the downstream jet contributing to upward motion over the landmass by means of its direct circulation at its jet entrance. The upstream jet during Type-N events induces downward motion over the southern half of South Africa as it propagates east. The Type-S upstream jet streak, which only appears during winter, has limited zonal extent and does not induce downward motion over the country. Type-N ridging is associated with stronger ageostrophic moisture fluxes along the southern coast leading to higher moisture content and precipitation along the south eastern and eastern coast of South Africa.

*Correspondence: thando.ndarana@up.ac.za

Keywords: Ridging highs pressure systems, jet streaks, Rossby wave packets, ageostrophic moisture fluxes

1. Introduction

Except for the winter and all season rainfall regions of the southwestern Cape and Cape south coast of South Africa (Weldon and Reason, 2014; Engelbrecht et al., 2015), most summer rainfall over South Africa occurs in the northeastern parts of the country (Roffe et al., 2019). It exhibits a strong zonal gradient, with highest totals over the eastern escarpment (de Coning, 2013; Dedekind et al., 2016; Roffe et al., 2019). Some of this rainfall is caused by cut-off low (COL) pressure systems (Favre et al., 2013) which occur right through the year with peaks during the transition seasons (Singleton and Reason, 2007a; Favre et al., 2013). As a result they contribute to annual precipitation the most during Spring (Favre et al., 2013). They are also contribute about 16% to the all seasons rainfall region of the Cape south coast (Molekwa et al., 2014; Engelbrecht et al., 2015). Furthermore, a large portion of the summer rainfall is brought about by the alignment of upper-level westerly waves over South Africa and tropical disturbances over the northern Namibia and southern Angola regions so that northwest to southeast orientated cloud bands occur (Harrison, 1984, Hart et al., 2012), which characterises tropical-extratropical interactions. These are locally referred to as tropical-temperate troughs (TTTs). During these cloud band events, patterns of outgoing long wave radiation (OLR) anomalies (Fauchereau et al., 2009; Ratna et al., 2013; Macron et al., 2014) that characterise the TTTs structure. These tropical-extratropical interactions are actually a global phenomenon, and in the Southern Hemisphere have been identified in South America (Liebmann et al., 1999; Zilli and Hart, 2021) and across the Australian continent (Reid et al. 2019). Over South Africa, they contribute more than 30% of the climatological rainfall from October to March with a contribution that is closer to 40% for the middle of the wet season (Hart et al., 2013). The prevailing OLR anomaly patterns are characterised by negative (positive) anomalies over South Africa (Madagascar) that signal enhanced (suppressed) convection (Waugh and Funatsu, 2003; Hart et al., 2013). In addition, smaller scale systems such as mesoscale convective complexes make up about a 20% contribution to summer rainfall (Blamey and Reason, 2012). The South African summer rainfall may also be contributed to by random air mass thunderstorms, as well as the Angola low (Reason and Jagadheesha, 2005; Munday and Washington, 2017; Howard and Washington, 2018; Howard et al., 2019). Under certain conditions the latter may migrate southward as a continental tropical low, and can cause heavy rainfall to occur over the country (Webster, 2018).

A critical component of the above is how moisture is transported to where rainfall occurs. Some of the moisture originates from the tropical South Atlantic (Vigaud et al., 2007; Rapolaki et al., 2020) and western Equatorial Indian (D'Abreton and Tyson, 1995) oceans, and is transported south towards South Africa along the axis of TTTs (Todd et al., 2004; Hart et al., 2010; Ratna et al., 2013; Macron et al., 2014). Rapolaki et al. (2020) also showed that moisture that affects the South African domain originates in the subtropical South Atlantic Ocean, the southwestern Indian Ocean waters located adjacent to land and further afield east of Madagascar. Central to moisture transport into South Africa is the ridging South Atlantic Ocean high (SAOH) pressure (simply referred to as the "ridging high"), which is not in itself a convective rainfall producing system. It does, however, cause some rainfall along the Cape south coast, as well as the east coast and eastern escarpment due to orographic effects (Engelbrecht et al., 2015). In some cases ridging events may be linked to COL pressure systems to cause extreme rainfall some parts of South Africa, leading to floods (e.g. Trigaardt et al., 1988; Singleton and Reason, 2006). All of this, combined with the fact that it contributes to the moisture budget of the region (Cook et al., 2004; Dyson, 2015; Engelbrecht et al., 2015; Ndarana et al., 2021a) renders the ridging high one of the most important synoptic weather systems in the South African domain. The ridging of the subtropical high pressure system is, however, not unique to the South Atlantic Ocean/South African sector. They have also been observed, for instance, in the Australian region. In that part of the Southern Hemisphere, Rehman et al. (2019) showed that the Indian Ocean anticyclone also ridges to impact the variability of precipitation over Tasmania, Australia.

During the ridging process, SAOH extends east and curves around the southern tip of the country, to first cause a south westerly on shore flow to enter the southern and south eastern coastal areas. At the later stages of the evolution of the ridging process, the flow becomes south easterly and transports moisture from the South West Indian Ocean (SWIO) (Cook et al., 2004; Dyson, 2015; Rapolaki et al. 2020; Ndarana et al., 2021a) into the eastern half of South Africa. The nature of this moisture transport is more clearly seen when the flow is decomposed into its geostrophic and ageostrophic components. Ndarana et al. (2021a) showed that the ageostrophic moisture fluxes mostly occur south of the 30°S latitude line and this moisture appears to originate from the SWIO waters that lie adjacent to the landmass. The geostrophic fluxes enter the country further north, just south of the Mozambique Channel, consistently with the location of the Mozambique Channel trough (Barimalala et al., 2018). Some of the moisture flux turns anticyclonically after entering the mainland and another branch appears to turn cyclonically. The latter affects the northern parts of South Africa and can reach further afield in Botswana and Namibia.

The SAOH pressure system ridges from the South Atlantic Ocean following the passage of a cold front (Tyson and Preston-Whyte, 2000; Ndarana et al., 2018). During the winter time, these cold fronts could bring cool temperatures over the country, which can cause low freezing levels and snow can occur (Stander et al., 2016), if there is sufficient uplift that is induced by orography and sometimes associated with westerly waves including COLs. For the Cape south coast of South Africa, there is evidence that topographic lift is an important contributing factor to ridging highs being associated with 46% of the rainfall occurring in this region (Engelbrecht et al., 2015).

Crimp and Mason (1999) conducted a case study of a ridging high that was involved in an extreme precipitation event. Fig. 2 of that study shows a ridging high centred south of 30°S with the ridging component that moved south from the SAOH, and moving around the country in an anticyclonic fashion, before amalgamating with the Mascarene high in the Indian Ocean (Xulu et al., 2020). A ridging high of this type has a strong meridional extent and may cause cold air outbreaks and heavy falls of rain such as sometimes observed along the east coast (e.g. Jury, 2018). An example of this type of ridging was observed during the September 1987 floods that occurred over the eastern parts of South Africa and were particularly devastating in the Durban area (Trigaardt et al. 1988; van Heerden and Taljaard, 1998). This structure of the ridging high is different from the composites that were produced in Ndarana et al. (2018). This suggests that whilst most ridging high pressure systems may have a zonal structure; some of ridging events, even though fewer in frequency as suggested by the dominant composite shape in that study, exhibit deviations from it and might reveal different characteristics of the ridging high process, as a result. Therefore the overall aim of this paper is to document the differences between the two types of ridging highs observed in the South African domain. The questions being asked are

- What is the structure of upper-level dynamical processes associated with the two types of ridging highs?
- What are the processes responsible for vertical uplift during ridging high pressure systems?
- What is the impact of the different types of ridging high on moisture transport?

The rest of the paper is structured as follows, in the next section the data and methods will be outlined, followed by a brief review of baroclinic wave processes and jet streaks of the Southern Hemisphere. The results section beginning with Subsection 4.1 presents the characteristics of the different types of ridging, followed by a discussion of the Rossby wave packets associated with them in Subsection 4.2 and the associated upper-level jet streaks in Subsection 4.3. In Subsections 4.4 and 4.5 implications on the vertical circulation and precipitation are drawn and finally the conclusions are presented in Section 5.

2. Data and Methods

2.1. Data

To identify ridging SAOHs, we use the fifth generation European Centre for Medium-Range Weather Forecasts Reanalysis (ERA5) from 1979 to 2020 (Hersbach et al., 2020). The horizontal grid spacing of each dataset is 2.5° at 6-hourly time intervals. Even though these products are available at much finer mesh grids and temporal resolution than this, we deem the chosen grid spacing sufficient because ridging high pressure systems are synoptic scale processes, the horizontal scale of which is $\sim 10^6$ m (Holton and Hakim, 2014). A sensitivity test showed that no significant advantage is achieved by using higher resolution data to identify these synoptic scale process and so to save on computational cost the chosen resolution is justified. The variables used are mean sea level pressure (MSLP), the temperature fields, the zonal and meridional wind components, geopotential heights to calculate the geostrophic $(u_g\mathbf{i} + v_g\mathbf{j})$ and ageostrophic $(u_a\mathbf{i} + v_a\mathbf{j})$ wind fields, the specific humidity (q) and vertical velocity ω. Even though we use 2.5° fields to identify ridging events; to diagnose vertical motion associated with them over the South African mainland, higher resolution ω fields are deemed better so that the vertical circulation induced by the dynamical processes associated with ridging highs and topography is better represented. For this purpose, 0.25° resolution ω and and specific humidity fields are used. In this study we assumed a variable f geostrophic flow (Blackburn, 1985) so that it is not non-divergent (Cook, 1999). We also use CPC Global Unified Precipitation data provided by NOAA/OAR/ESLR PSD, Boulder, Colorado, USA that is provided on a 0.5° horizontal grid spacing.

2.2. Methods

Ridging highs are objectively identified using a simple algorithm consisting of three steps. Its details are provided in Ndarana et al. (2018) and only a brief description is provided here. In the first step, we identify closed contours in the 6-hourly MSLP fields are identified within a domain bounded by 40°W and 60°E, and Equator and 50°S and keep only those whose MSLP value at the centre is higher than that at around the contour. We then group these closed contours so that concentric contours in the South Atlantic Ocean represent the SAOH. This is the second step. In the third and final step, if the outermost contour extends east of the 25°E longitude line, we record such instances as the ridging process having occurred. If this condition is met on consecutive time steps, without any breaks in between, then this constitutes a single ridging event. The number of six-hourly time steps that this condition is met is then considered to be the duration of the ridging events.

In addition to categorising the events on the basis of duration, a further categorisation is implemented. To do this we select only those events that have a duration longer than a day. This is informed by the fact that the time scale of synoptic processes is $L/U \sim 10^5$ s and rainfall over the eastern parts of the country is mostly influenced by longer lived events. Furthermore, many of the shorter lived ridging might not evolve across South Africa to exhibit the behaviour of interest in this study. Recalling that pressure increases in the SAOH from the outer most isobar towards the inner most one and that the isobars that form the high are concentric, the centre, (λ_c, ψ_c), of the system is the centre of the closed contour that has the highest MSLP value. To estimate the position of the centre of a ridging event we then take the average longitude and latitude of the SAOH as it ridges and consider that the centre of ridging high. ψ_c then defines the latitude at which a ridging event occurs. Based on the resolution of the reanalysis data used in this study, the events are then grouped according to $\psi_i < \psi_c < \psi_{i+1}$, where $\psi_{i+1} = \psi_i + \delta\psi$, $\delta\psi = 2.5°$ and $\psi_1 = 90°$S. We then calculate the average MSLP fields across each group at t = +24 hours. A visual inspection of these average fields shows that north of the 40°S latitude line, the ridging events are more zonal and behave in the manner presented in Ndarana et al. (2018). We call these Type-N ridging events. South of this latitude line, ridging exhibits completely different behaviour. Such events are referred to as Type-S.

To establish the climatological behaviour of the ridging events and associated fields, composite means are used. In preparation for the composite calculations, the events are categorised into Type-N and Type-S types, as defined above. Sun et al. (2017) showed that the SAOH exhibits strong seasonality, as such we further subdivide the different types of ridging events into seasons. Furthermore, only events of duration longer than 24 hours are considered for the calculation of the time-lagged composites. To calculate these, the following steps are implemented:

1. For each event in each category, $t = 0$ is the time step at which the ridging process is first detected. For example, if one event in a category occurs on 01 January 2011 06h00 and another is identified at 03 February 2011 at 18h00, etc, then all the fields associated with these events are averaged. Critical t values of perturbations fields are also calculated using the method of Brown and Hall (1999), to establish statistical significance. This produces composite means for the time lag $t = 0$ hours.
2. This process is repeated for the rest of the time steps backward and forward in time in six hourly intervals. This produces composite means for t = -48, ..., -12, -6, 0, +6, +12, ..., +48 hours.

These composite calculations then produce composite evolutions of Type-N and Type-S types of events and all fields considered in the study for each season.

3. Review of a baroclinic wave processes and jet streaks

The dynamics associated with most South African weather systems are dominated by the Rossby wave packets (RWPs) (e.g. Ratna et al., 2013, O'Brien and Reeder, 2017; Ndarana et al., 2018, 2021a) and jet streaks (e.g. Ndarana et al., 2021b). So a brief review of the dynamical processes involved in a propagating baroclinic wave and the jet streaks embedded in it would be instructive in assessing the differences between the upper-level dynamics that accompany the evolution of different types of ridging high events.

As far back as Lee and Held (1993) RWPs have been diagnosed using v', which is the perturbation meridional velocity field. It is defined as a deviation of the meridional flow from some basic state, that would either be the zonally symmetric or time symmetric (or more generally slowly varying) flow. This is represented schematically in Fig. 1 (a) by the closed elliptical non-shaded shapes and the blue (red) oval shaped contours are the $v' > 0$ ($v' < 0$) fields, relative to the vorticity maxima. $v' < 0$ is located between the trough axis (straight black line) and the ridge axis (dashed line) immediately downstream of it. We will refer to this trough as the "main trough". Its minimum values are located at the inflection point, which is where upward vertical motion (blue shaded area) also occurs. The upward vertical motion here is induced by the divergent ageostrophic flow, as required by the conservation of mass. In the Southern Hemisphere a trough is curved northward whilst the ridge is curved southward. The flow across the relative vorticity minimum (trough) and relative vorticity maximum (ridge) in the sinusoidal baroclinic wave structure is subgeostrophic (thick blue arrow) and supergeostrophic (thick black arrow), respectively (Orlanski and Sheldon 1995). Therefore the ageostrophic flow across the trough axis will be directed in the opposite direction of the flow (curved purple curve). The ageostrophic flow (curved red arrow) across the ridge axis points downstream, in the opposite direction. This creates a flow divergence region which is a maximum at the inflection point of the wave, located between the upstream trough axis and the ridge axis immediately downstream, where $v' < 0$ is a minimum. The ageostrophic flows across the ridge axis and the trough axis downstream converge at the inflection point between the two axes and induce downward motion there ($\omega > 0$).

The vertical motion patterns are also associated with the divergence and convergence structures of the jet streak (Fig. 1(b)). At the jet entrance and exit there are thermally direct and indirect circulations, respectively. Therefore, when presented in the context of the baroclinic wave, the location of the downstream jet streak (hatched oval shape in Fig. 1(a)) is consistent with the regions of ageostrophic flow divergence and convergence at the inflection points because of the transverse circulations just discussed (Uccellini and Kocin, 1987). For South Africa and the surrounding oceans, the position of the jet streak is informed by Ndarana et al. (2020, 2021b), who found that this jet streak is responsible for inducing anticyclonic wave breaking and the associated ageostrophic geopotential fluxes that transport eddy kinetic energy in a northeasterly direction from the midlatitudes to cause downstream development during the evolution cut-off low pressure systems. Fig. 1(a) also includes the possibility of another jet streak that is located upstream. In the Northern Hemisphere this double jet streak structure is oriented differently (Uccellini and Kocin, 1987). The upstream jet is poleward so that it couples to its downstream counterpart by means of the thermally indirect circulation at its exits, so that upward motions occurs between the jets. Here, there is downward motion between the jets.

4. Results

4.1. Type-N and Type-S ridging highs

A total of 2423 ridging events were identified from 1979 to 2020 and 578 (24%), 617 (25%), 577 (24%), 651 (27%) of them occur during the summer (DJF), autumn (MAM), winter (JJA) and spring (SON) months, respectively. Fig. 2 shows the frequency of occurrence of the events as a function of latitude of the centre of the high. Fig. 2 categorises the frequency of events into those that occur north of the 40°S latitude line (red bars) and those that occur south of it (black bars) for each season. These were referred to as Type-N and Type-S ridging events in Section 2.2. A total of 467 (111), 449 (168), 517 (60) and 522 (129) Type-N (Type-S) events were identified during DJF, MAM, JJA and SON, respectively. The seasonality of the frequency of the ridging events exhibits the same behaviour that has been observed for other metrics of the SAOH, such as its intensity (Sun et al. 2017).

As noted, Type-S and Type-N events show very different evolution characteristics. This behaviour is presented as composite fields in Fig. 3 for DJF. From Fig. 2, 467 (111) cases were used for calculating Type-N (Type-S) composite fields. The left panels of Fig. 3 show the time-lagged composite evolution of MSLP fields and their anomalies that are significant at the 95% level for Type-N events. These are similar to the composites presented in Ndarana et al. (2018, 2021a) and most commonly observed by forecasters from National Meteorological Services in southern Africa. The ridging process is zonal in structure, and as expected, it is confined to latitudes north of 40°S. The SAOH extends eastward and, as shown in Ndarana et al. (2018), the leading edge of this extension then separates itself from the parent anticyclone and rolls off across South Africa. As it does so, it decreases in strength and eventually amalgamates with the Indian Ocean high pressure system. Note that the maximum

MSLP values of the SAOH remain in the South Atlantic Ocean and do not propagate across South Africa, as though the land mass bars it from propagating eastward. Type-S events evolve in a very different manner (right panels of Fig. 3). In their case, the maximum MSLP values of the SAOH extends to the south of the land and as the leading edge cuts off, the smaller scale high pressure system that forms as a result thereof increases significantly in strength. This is very clearly indicated by the statistically significant MSLP anomalies, represented by the orange to red shading, which is much stronger than the anomaly structure that is associated with Type-N events (as indicated by the difference in shading) in the corresponding panels. Note that the inclusion of MSLP anomalies highlights the differences between the behaviour of the two types of ridging more clearly. Clearly then, Type-S events and their MSLP anomalies remain south of the country as they propagate east and the anticuclones eventually combine with the Indian Ocean anticyclone, as was the case with Type-N events.

The difference in the strength and behaviour of the small scale high pressure systems that breaks off from the parent SAOH during for Type-N and Type-S events is one distinction to make between the two types of ridging, as noted above. The other distinction to make is that Type-N events start off with a stronger SAOH pressure system, as indicated by the presence of the thick blue contour, which represents the 1022 hPa MSLP isobar in the composite mean at t = -12 hours in Fig 3 (a). This thick blue contour is absent in the corresponding time steps during the composite evolution of Type-S events in Fig. 3(g), showing that the MSLP values are lower than 1022 hPa. The Type-N SAOH remains stronger than the one associated with Type-S events as shown by the hatches in the South Atlantic Ocean (see right panels in Fig.3) right through the evolution of the composite events. The hatched regions indicate where Type-S MSLP subtracted from Type-N MSLP is positive, thus showing that the MSLP of Type-N events is higher. The other difference to note here is the orientation of the isobars that enter eastern coast of South Africa. They are more perpendicular to the coast in Type-S events than it is the case for Type-N ridging highs. This might have profound implications for moisture transport and cold air intrusions into the continental interior as far north as Zimbabwe. In fact most of the episodes of cold air intrusions are associated with some kind of ridging process. Finally, to assess the seasonal variation in the structures of the two types of ridging, Fig. 4 shows the MSLP and their anomalies for (a,e) DJF to (d,h) SON. The increase in size of the 1022 hPa thick blue contour show that MSLP increases from the warmer to the colder months of the year. This increase is evident in the MSLP anomalies as well.

4.2. Rossby wave packets associated with Type-N and Type-S ridging

Evidence of the existence of RWPs, and broad over view thereof, during the evolution of Type-N (left panels of Fig. 5) and Type-S (right panels Fig. 5) ridging events is presented in the form of a Hovmöller diagram for DJF (top panels of Fig. 5) and JJA (top panels of Fig. 5). These graphs were produced by taking the average of composite fields of v' between 60°S and 35°S. This shows that Rossby wave trains develop in the vicinity of South America (60°W), prior to the onset of the ridging process at t = 0 hours, and then propagate in the general eastward direction towards the South African domain, as in O'Brien and Reeder (2017). Even though the Hovmöller plot does not provide the two dimensional structure of the wave trains, as it is constructed by taking the meridional average, it does provide a succinct picture of the differences between the wave structure associated with the two types of ridging events. Comparing Figs 5(a) and (b) shows that the RWP associated with Type-N matures at the point at which the ridging process is initiated, whist those associated with Type-S mature later (above the solid line going through solid line at $t = 0$). The latter also propagates farther downstream beyond the South African domain for longer and also have larger amplitude. Type-S RWPs also develop downstream of the location of the region where Type-N packets first appear. From these Hovmöller plots there is no evidence of an influence from the South Pacific Ocean (west of dotted red line which represents the location of 60°W) and the trough that influences the South African domain as the ridging process is initiated develops in the South Atlantic Ocean. Similar differences between RWPs associated with the the two types of ridging are also observed for the winter time systems (bottom panels of Fig. 5).

However the RWP associated with both types of ridging appear to dissipate a little earlier during the winter.

We now expand the composite mean fields shown in the top panels of Fig. 5 for DJF to two dimensions and then superimpose the MSLP anomalies (as in O'Brien and Reeder, 2017), and select MSLP isobars (i.e. 1018 and 1022 hPa contours). The meridional perturbation velocity fields are not shaded as in Fig. 5 but are represented as suggested by Fig. 1(a) instead, so that they may be interpreted using that schematic as guidance. All these fields are shown in Figs 6 for DJF from t = -72 hours (i.e. 3 days prior to the initiation of the ridging process) in 24 hour intervals to t = +48 hours, and note the thick black curve at t = +24 hours (Figs 6 (c) and (i)), representing the position of the main trough, as noted in Section 3. As Fig. 5 suggests, the $v'(\lambda, \phi, t)$ field has no clear structure, prior to t = -72 hours (not shown) and so we first present a description of the state of the relevant atmospheric variables from this point (i.e. Figs 6 (a) and (g)). At the lower levels, there is a pre-existing positive MSLP anomaly that is located near 30°W. For some composites of different seasons, for instance MAM and SON (not shown), it is located slightly east of this latitude line. Near the Greenwich Meridian there pre-exists a negative anomaly, which might be associated with the cold front, behind which the leading edge of the ridging high trails (Tyson and Preston-Whyte, 2000). The positive MSLP anomaly develops to become much stronger for Type-S events beyond t = 0 hours.

The initiation of the development of the wave packet is marked by the general eastward propagations of the positive MSLP anomaly, which was considered in the previous section but discussed here in the context of propagating Rossby waves. In the case of Type-N events (left panels of Fig. 6), it is advected in a north-easterly direction, and eventually forms part of the ridging. As soon as it enters the SAOH, it propagates eastward together with the leading component of the ridging high and increases in pressure fields that are induced by the ridging process, as the SAOH extends eastward. The right panels of Fig. 6 show that in the case of Type-S ridging events, the advected positive anomaly propagates in a more zonal manner. It intensifies significantly and becomes much stronger than its Type-N counterpart, as it propagates past the South African domain. For this reason, the MSLP in Marion Island increases, and at the same time the Indian Ocean high pressure system shifts eastward, thus decreasing the MSLP in St. Brandon. This leads to a positive phase of the Brandon-Marion Index (BMI) (Rocha and Simmonds, 1997a), so that the main trough (represented by the thick black contour in Fig. 6 (c,i)) is located over South Africa, as the ridging process brings moisture into country (Cook et al., 2004; Dyson, 2015; Ndarana et al., 2018). This results in rainfall over the summer rainfall region. One may then suggest that the relationship between the BMI and South African rainfall discovered in Rocha and Simmonds (1997a) is supported by the dynamics associated with ridging highs. In an accompanying study, Rocha and Simmonds (1997b) further showed that sea surface temperatures (SSTs) patterns in the Indian Ocean have a profound impact on the precipitation of South Africa. In particular, positive anomalies in some parts of the ocean are correlated with dry conditions over the country, because these anomalies are associated with reduced moisture onshore fluxes. Whereas, positive anomalies in the southwestern Indian Ocean are linked to wet conditions over the country (Reason and Mulenga, 1999). Because the SSTs affect the South West Indian Ocean moisture fluxes, which have been established to be caused by the ridging process (Ndarana et al. 2021a), it is plausible then that ridging highs may be one of the mechanisms that explain this association between the Indian Ocean SST variability and South African rainfall. This hypothesis requires further investigation.

As these positive anomalies propagate eastward in the manner described above, ahead of them the cold-front-induced negative anomaly deepens and propagates east, as well. Behind the positive anomalies a region of negative anomalies develops just east of 40°W and at about 45°S. This is a well known centre of cyclogenesis (e.g. Reboita et al., 2010), which is observed for Type-N events for all seasons. O'Brien and Reeder (2017) found a similar process for RWPs associated with jet interactions. For Type-S events this a negative MSLP field is found across Drake Passage, covers the Antarctic Peninsula into the Weddell Sea. This is one of the regions of high cyclonic activity around in Antarctica (Simmonds et al., 2003). The anomaly also intensifies because the surface pressure depression deepens beyond cyclogenesis, as one would expect.

These surface processes give rise to (or are associated with) a trough/ridge system aloft. Immediately west of the negative MSLP anomalies there are trough axes (the contour at which v' changes from positive (blue contours) to negative (red contours) values), as suggested in the schematic in Fig. 1(a), with the thick black contour in Figs 6 (c) and (i) representing the main trough. Similarly, west of the positive MSLP anomalies there are ridge axes. Therefore the wave lags westward with height, a clear signature that it is baroclinically unstable. The first difference between the Rossby wave propagation that is associated with the two types of ridging is that the main trough reaches South Africa earlier for Type-N events. The second difference between the upper-level structures is that the speed of the northward excursions of air parcels west of the main trough is much stronger for Type-S events. This is consistent with the stronger negative MSLP anomaly. The upstream southward velocity fields are also stronger for Type-S, which is again consistent with the stronger positive MSLP anomaly. Rossby waves associated with both types of ridging are therefore baroclinic but evolve very differently. This has deep implications for the baroclinic conversion of eddy available potential energy to eddy kinetic energy. The diagnosis of the mechanisms involved in their development and eastward propagation are the subject of a follow up study to the current one, however it is worth noting here that the downstream development process similar to that identified for cut-off low pressure systems in this domain (Ndarana et al., 2021a) should play a critical role here.

It now remains to be determined where the strength of the Type-S positive anomaly originates from and also consider the seasonal differences of this effect. Many studies, following Hoskins et al. (1985), have used potential vorticity (PV) inversion to study various atmospheric dynamical processes, examples of which are frontogenesis (Morgan, 1999), the relationship between PV intrusions and convection (Funatsu and Waugh, 2008), the effect of precipitation on downstream mesoscale processes (Baxter et al., 2011) and extreme weather phenomena such as typhoons (Wang et al., 2020), to name a few. Based on the usefulness of PV inversion (Røsting and

Kristjánsson, 2012), Barnes et al. (2021) conducted a systematic idealised PV inversion experiment to show that the strength or intensity of a PV anomaly leads to a more intense circulation around it. They also showed that when a PV anomaly is on a lowered tropopause height, it will also be associated with a stronger circulation at the surface. Even though these experiments focused on high (i.e. negative) PV anomalies, the same may be inferred for positive anomalies. Fig. 7 shows the meridional cross-section of PV anomaly (shading), PV = -2PVU (thick dashed blue) contour representing the dynamical tropopause, and the geopotential height anomaly (thin black and red contours) for DJF to SON from the top to the bottom panels. Using the Barnes et al. (2021) result, it is clear in Fig. 7 that the positive PV anomaly induces a stronger anticyclonic response for Type-S ridging events and that this response is weakest in summer and strongest during the winter months. In addition, the deeper Type-S anomaly is associated with a lowered tropopause level during all seasons, which is also associated with more intense surface circulations. All these factors contribute to the stronger MSLP anomalies shown in the right panels of Fig. 6. These findings are consistent with the Barnes et al. (2021) experiments.

4.3. Upper-level jet streak structures and low-level thermal processes

The previous section considered the development and propagation of the RWPs that occur during the two types of ridging events in order to establish the nature of the associated upper-level dynamical processes. In this section and the next we contrast the upper-level jet streaks that materialise and consider their possible implications for upward motion over the South African mainland. Fig. 8 shows that the two types of ridging are associated with differential 250 hPa jet streaks (shading in Fig. 8) configurations for DJF. Type-N events have a clear double jet structure (i.e. the shaded zonal wind component at 250 hPa) associated with the ridging process, with the upstream jet established before the ridging process commences and located south of the parent SAOH. By the thermal wind relation invoked at 600 hPa, it is associated with $\partial_y T > 0$ at 600 hPa (thin black solid contours in Fig. 8). This upstream jet streak extends eastward and increases in strength (or appears to be translated eastward) as the ridging process evolves, by the redistribution of zonal momentum from the jet entrance eastward by advective processes (Ndarana et al. 2020). This eastward extension of the jet appears to be associated with the ridging process, as the two appear to be correlated. The right panels of Fig. 8 show that the upstream jet that is associated with Type-S ridging events is not significant but it does appear more clearly during the winter months (not shown). It is more zonally constrained than its Type-N counter part and appears much later in the sequence of events; after the ridging process has commenced. It also develops further downstream, south of the ridging component of the SAOH, which is also more zonally constrained.

Both types of events have a downstream jet that is oriented in a similar fashion associated with them. In both cases the jet is caused by the temperature gradient that is associated with the cold front ahead of the ridging high (see Section 1), as it brings cold air in the south westerly flow in its wake. The southern Agulhas Current including its retroflection and the rings shed there may contribute towards this low-level temperature gradient as it waters are typically 5°C or warmer than the nearby ambient ocean (Lutjeharms, 2006; Loveday et al., 2014). Further downstream, the Indian Ocean high pressure system induces an anticyclonic circulation and heat fluxes that meet those that are caused by the cold front. Note that the direction of the flow behind the cold front is consistent with the ridging high and that is it is stronger for Type-S events, leading to a stronger heat flux for Type-S events. This is expected because the pressure gradient associated with Type-S events is much stronger than that is associated with Type-N events. This leads to a stronger temperature gradient and a stronger downstream jet as a result (as seen by comparing the isotachs in the left and right panels in Fig 8).

4.4. Upper-level flow and implications for the vertical circulation

The circulation patterns of jet streaks reviewed in Section 3 and the jet streak structures discussed in Section 4.3, their development and position relative to the country, as well the Rossby wave packets (or baroclinic waves) in which they are embedded (also reviewed in Section 3 and discussed in Section 4.2) all play a critical role in informing the patterns of vertical motion in and around South Africa. Fig. 9 shows the 250 hPa ageostrophic flow, and its divergence and convergence patterns relative to the jet streaks and Rossby wave patterns for DJF. We consider the effects of the upstream jet streak first. During the early stages of development (at t = -12 hours and 0 hours - Figs 9 (a) and (b) for Type-N and Fig 8 (g) and (h) for Type-S), the ageostrophic divergence is found close to the middle of the jet streaks, near the middle most point of the downstream jet streak, which is also the point of inflection in the baroclinic wave. As a result the flow is subgeostrophic at the top of the main trough (see Sections 3 and 4.2) just south-west of South Africa, as indicated by the direction of the ageostrophic flow there (as illustrated schematically by the purple curved arrow in Fig. 1(a)). At the bottom of the ridge, located south east of the inflection point in question the flow is clearly supergeostophic, where the ageostrophic flow would transport eddy kinetic energy downstream (Orlanski and Katzfey, 1991; Orlanski and Sheldon, 1993, 1995; Lackmann et al., 1999; McLay and Martin, 2002; Decker and Martin, 2005; Danielson et al., 2006; Harr and Dea, 2009; Ndarana et al., 2021b). This ageostrophic flow converges with that which is directed in a south-westerly direction more or less above the centre of the Mascarene high.

One very conspicuous difference between the upper-level flow structures that are associated with the two types of ridging is that the ageostrophic flow convergence found near the boundary of the South Atlantic and Indian Oceans evolves to be stronger for Type-S. This is clearly influenced by the fact that the diffluent super-geostrophic flow associated with the jet exit of the upstream jet streak is absent or weak during the evolution of these ridging highs. The ageostrophic component of this diffluent flow, of course, defines the thermally indirect transverse circulation at the jet exit of the upstream jet streak (see Fig 1(b)). In contrast, the large scale upstream jet streak found during Type-N events induces such anticyclonic diffluent flow so that the ageostrophic winds from the downstream trough and that associated with the jet exit and across the upstream ridge axis, partially converge and partially merge to be directed towards the north west. This combined flow converges with the ageostrophic flow from the north-east, which would be the upper-level component of the direct circulation associated with the downstream jet streak. The effect of this is a weaker but broader convergence zone that stretches further north-west than its Type-S counterpart. As Type-N events evolve, the northern parts of this ageostrophic flow convergence zone migrates eastward and invades the south-eastern and southern parts the South African landmass. Corresponding composites beyond t = 0 hours for Type-S events (Fig. 9 (j) to (l)) show that over South African there is ageostrophic flow divergence. This has profound implications for the vertical circulation over the country. As was the case with the other fields, the seasonal differences are presented only for t = +24 hours in Fig. 10. The flow convergence located at the boundary of the South Atlantic and Indian Oceans decreases in intensity from DJF to reach minimum values in JJA, whilst the jet upstream jet associated with Type-S increases in strength to become strongest in winter. The growing strength of the upstream jet streak from MAM to reach a maximum in JJA reduces the intensity of this convergence zone.

The vertical circulation response to the upper level divergence and convergence patterns of the flow is presented in Fig. 11, which shows high resolution composite 700 hPa ω mean fields (shaded) together with the jet entrance (250 hPa zonal isotachs represented by the black dashed contours plotted from 30 m s^{-1}). The ω fields are also plotted relative to topography (black contours). The effect of upper level ageostrophic flow convergence that develops over the south-eastern and southern parts parts of South Africa, is observed in the left panels of Fig. 11 for Type-N events is apparent. This is shown by the statistically significant $\omega > 0$ values in the left panels of the plot. This is impacted by the eastward movement of the jet streak as suggested by Fig. 1 and discussed above. The presence and evolution of $\omega < 0$ on the anticyclonic barotropic shear side of the jet streak is induced by the ageostrophic flow divergence that is shown in Fig. 9. During the early stages of the evolution of the ridging highs (see Fig. 3), the onshore low level flow (as indicated by the MSLP isobars) suggest that along the eastern coast, the $\omega < 0$ field could be induced by uplift due to orographic factors, as the flow is directed towards the escarpment (see black contours). The strong $\omega < 0$ field located on the lee side of the escarpment is most likely more dynamically induced by the presence of the jet streak. There significant differences between the vertically upward motion during the evolution of the two types of ridging events, particularly along the eastern coast. Consistently with the flow, it is longer lived for Type-S events than it is for Type-N ridging highs. Whilst this upward motion might be due to orographic, when extreme rainfall events occur along the eastern coast, they are usually associated with cut-off low pressure systems. However, regardless of how this vertical motion is induced, its strength and long loved nature for Type-N events suggests that the rainfall associated with these types of ridging events will be higher, as will be discussed further in the following section.

4.5. Implications for moisture fluxes, moisture content and rainfall

One way of diagnosing the ridging induced moisture fluxes from the South West Indian Ocean (SWIO) is to divide them into its geostrophic ($\mathbf{Q}_g$) and ageostrophic ($\mathbf{Q}_a$) components (Xue et al., 2018; Ndarana et al., 2021a). Fig. 12 shows the differences between precipitable water (ΔPW = PW(Type-S) - PW(Type-N)) and geostrophic moisture fluxes ($\Delta\mathbf{Q}_g = \mathbf{Q}_g$(Type-S) - $\mathbf{Q}_g$(Type-N)). The right panels show the differences between ageostrophic fluxes induced by Type-S and those associated with Type-N ($\Delta\mathbf{Q}_a = \mathbf{Q}_a$(Type-S) - $\mathbf{Q}_a$(Type-N)), as well differences between daily precipitation associated with the two types of ridging (ΔP = P(Type-S) - P(Type-N)). The positive values of ΔPW show that Type-S events are associated with a moisture content that progressively becomes stronger than that which accumulates during the evolution of Type-N events (left panels of Fig 12). Given lifting mechanisms caused by upper-level divergence that is associated with passing baroclinic waves (or Rossby wave packets or trains) and the jet streaks they bring along with them, Type-S events are associated with heavier precipitation than Type-N ridging events, on average. This is particularly true for the south eastern and eastern coasts, as shown by positive values of ΔP in right panels of Fig 12.

Differences in total flux $\Delta\mathbf{Q}$ (not shown) exhibit an off-shore resultant flux vector distribution that is similar to that of $\Delta\mathbf{Q}_g$ (represented by the grey vectors in the left panels in Fig. 12). In addition, Ndarana et al. (2021a) showed that $\mathbf{Q}_g$ is oriented parallel to the south eastern and eastern coasts of South Africa and only strongly cross the boundaries of the landmass much further north, in the Mozambique Channel and just south of it (cf. Fig 5 in Ndarana et al., 2021a). This is the case for both types of ridging events. It may then be concluded from this observation that it cannot be the geostrophic component of the wind that brings about the moisture content that results in the heavier rainfall that is associated with Type-S events. The right panels of Fig. 12 show that effective component of the wind that causes the differences in moisture content and precipitation between the two types of ridging events is the ageostrophic flow. The resultant ageostrophic flux ($\Delta\mathbf{Q}_a$, represented by the red arrows in Fig. 12) shows that Type-S events bring more moisture from SWIO across the south eastern and eastern coasts of South Africa.

The occurrence of precipitation also depends on the accompanying systems aloft. On several occasions, ridging anticyclones co-occur with heavy rainfall producing systems such as mid-tropospheric COLs and TTTs. Several studies found that intense COLs over South Africa were coupled to a ridging high near the surface (e.g Singleton and Reason, 2006; 2007b; Taljaard, 1985). Similarly, TTTs and attendant cloud bands are often coupled to a cold front at their southeastern end with a ridging high pushing behind as they propagate eastwards over South Africa (Hart et. al., 2010). Furthermore, when a COL is located near the coast, the interaction of a ridging high with the steep escarpment parallel to the coast enhances rainfall there due to orographic lifting (Weldon and Reason, 2014).

5. Concluding remarks

Using ERA5 data from 1979 to 2020, this study has identified and characterised two types of ridging high pressure systems that occur in the southern African domain. A ridging high is defined as a South Atlantic Ocean anticyclone that extends east so that the leading edge of that extension breaks off and is combined with the Indian Ocean high pressure system. The characterization of these two types of ridging highs is motivated by forecasting experience at the South African Weather Service (in a addition to a few case studies of heavy rainfall in the domain) that suggests that there might be differences in the severity of the rainfall associated with them. Type-N ridging events are defined as those events that occur on and north of the 40°S latitude line and Type-S events occur south of it. The latitudinal distribution of the different types of ridging exhibit strong seasonality. The distribution of Type-N and Type-S is similar during the transition seasons. During the colder months of the year, Type-S events are at a minimum.

There are very clear structural differences between the two types of ridging events. Type-N events have, on average, a more zonal structure and the leading edge that breaks off to form the small scale high pressure system is relatively weak, leaving behind a relatively strong anticyclone in the South Atlantic Ocean. This means that the maximum mean sea level values associated with Type-N remain in the South Atlantic Ocean. In contrast to this, Type-S events appear to extend southward, so that their structure is less zonal. The small scale high pressure system that forms south of the country and breaks off is much stronger than its Type-N counterpart and leaves behind a much weaker circulation in the South Atlantic Ocean. As opposed to Type-N, the maximum values of mean sea level pressure propagate east and are not confined to the South Atlantic Ocean. The structure of the two types of ridging exhibit seasonal variations. Sun et al. (2017) showed that the intensity of the subtropical anticyclone increases from summer to winter, as such, the ridging high studied here induce higher mean sea level pressure anomalies during the colder months of the year.

Both types of ridging events trail behind a cold front, which in turn, causes positive meridional temperature gradients in the lower levels of the troposphere, thus giving rise to a downstream jet streak. As the two types of ridging evolve, the middle most point of this jet streak is located at the inflection point east of the upper-level trough axis, where upper-level divergence of the ageostrophic flow and hence vertical upward motion is a maximum over the South West Indian Ocean waters. The entrance of the jet is located just south of the country, and it is also co-located with the upper-level subgeostrophic flow found across the trough axis. This is consistent with the ageostrophic flow observed there, so that the direct transverse circulation of the jet streak contributes to the flow divergence over South Africa. The downstream jet structure and upper-level dynamics associated with it are broadly similar in both types of ridging, except the jet is stronger for Type-S events, as informed by the stronger temperature gradient. The difference in the upper level jet structures between the two types of ridging is that Type-N is associated with a very well defined upstream jet that extends east as the ridging process evolves. Type-S events are associated with a smaller scale jet streak that is weak in summer and becomes strongest in winter.

The jet streaks are embedded in the Rossby wave packets that propagate across the South Atlantic Ocean, past the South African domain and dissipate in the Indian Ocean. These wave packets associated with the different types of ridging highs propagate towards South Africa in a similar fashion, along established waveguides (Hoskins and Ambrizzi, 1993; O'Kane et al., 2016). The rear end of these baroclinic disturbances maybe induced or enhanced by cyclogenesis that is climatologically located in the middle of the South Atlantic Ocean, whilst their leading edge is maintained by the cold fronts that are associated with the ridging highs, which also give rise to the jet streak located at that part of the wave. At the centre of the Rossby wave there is a low-level positive geopotential height anomaly, and its north easterly (in the case of Type-S events) and easterly (in the case of Type-S events) marks the beginning of the propagation of the Rossby wave packets in the South Atlantic Ocean. It is much stronger in the Type-S case and this strength might be linked to stronger potential vorticity anomalies, as suggested by recent potential vorticity inversion experiments conducted for the South African domain (Barnes et al. 2021). This is consistent with the fact that Type-S events occur in regions of stronger baroclinicity (Simmonds and Li, 2021), than Type-N. The magnitude of the anomalies of the baroclinic wave increase with season from summer to winter consistently with the seasonal behaviour of the baroclinicity.

Type-S events are associated with higher moisture content in some parts of South Africa, particularly of interest, along the eastern coasts of the country. This is caused by their stronger ageostrophic fluxes that are induced by the tighter pressure gradients observed in the ridging component of the SAOH. When this is considered together with the fact that the vertically upward motion associated with Type-S is stronger, aided by the fact that the upstream jet streak that has the opposite effect is too far south and too small (as it is case with Type-N events), heavier rainfall appears to occur during these events.

This study has highlighted the need to consider the nature of the influence that topography has on the flow during the evolution of ridging highs. This will be addressed in a follow up study to test the hypothesis that the upward velocity field on the lee side of the escarpment is induced by dynamical processes that are associated with streaks. The follow up study will also address the issue of orographic vs. dynamical uplift on the eastern side of the escarpment, when the ridging high is accompanied by strong systems such as cut-off lows.

Acknowledgements This work is part of a broader project that, whose aim is to understand that the underlying processes of the important synoptic systems in the South Atlantic Ocean/South Africa basin. The authors would like to the Water Research Commission (Grant number: C2020/2021-00653) for its support. A heartfelt gratitude also goes out to the anonymous reviewers who constructively assessed the work.

References

[1] Barnes, M.A., Ndarana, T., Sprenger, M. Landman, W.A., 2021. Stratospheric intrusion depth and its effect on surface cyclogenesis: An idealized PV intrusion experiment. Weather. Clim. Dynam. Submitted. https://doi.org/10.5194/wcd-2021-24.

[2] Barimalala, R., Desboilles, F., Blamey, R.C., Reason, C.J.C., 2018. Madagascar influence on the South Indian Ocean convergence zone, the Mozambique Channel trough and southern African rainfall. Geophys. Res. Lett. 45, 11380-11389. https://doi.org/10.1029/2018GL079964.

[3] Baxter, M. A., P. N. Schumacher, J. M. Boustead, J. M., 2011. The use of potential vorticity inversion to evaluate the effect of precipitation on downstream mesoscale processes. Q. J. R. Meteorol. Soc. 137, 179-198. https://doi.org/10.1002/qj.730.

[4] Blackburn, W., 1985. Interpretation of ageostrophic winds and im-

plications for jet stream maintenance. J. Atmos. Sci. 23, 2604-2620.https://doi.org/10.1175/1520-0469(1985)042¡2604:IOAWAI¿2.0.CO;2.

[5] Blamey, R.C., Reason, C.J.C., 2012. Mesoscale convective complexes over southern Africa. J. Climate. 25, 753-766.https://doi.org/10.1175/JCLI-D-10-05013.1.

[6] Brown, T.J., Hall, B. L., 1999. The use of t values in climatological composite analyses. J. Climate. 12, 2941-2944.https://doi.org/10.1175/1520-0442(1999)012¡2941:TUOTVI¿2.0.CO;2.

[7] Cook, K.H., 1999. Generation of the African Easterly jet and its role in determining west Africa. J. Climate. 12, 1165-1183. https://doi.org/10.1175/1520-0442(1999)012¡1165:GOTAEJ¿2.0.CO;2.

[8] Cook, C., Reason, C.J.C., Hewitson, B.C., 2004. Wet and dry spells within particularly wet and particularly dry summers in the South African summer rainfall region. Clim. Res. 26, 17-31. https://doi:10.3354/cr026017.

[9] Crimp, S.J., Mason, S.J., 1999. The extreme precipitation event of 11 to 16 February 1996 over South Africa. Meteor. Atmos. Phys. 70, 29-42. https://doi.org/10.1007/s00703005002.

[10] Danielson, R.E., Gyakum, J.R., Straub, D., 2006. A case study of downstream baroclinic development over the North Pacific Ocean. Part II: diagnoses of eddy energy and wave activity. Mon. Wea. Rev. 134, 1549-1567. https://doi.org/10.1175/MWR3173.1.

[11] D'Abreton, P.C., Tyson, P.D., 1995. Divergent and non-divergent water vapour transport over southern Africa during wet and dry conditions. Meteorol. Atmos. Phys. 55, 47-59. https://doi.org/10.1007/BF01029601.

[12] de Coning, E., 2013. Optimizing satellite-based precipitation estimation for Nowcasting of rainfall and flash flood events over the south African domain. Remote. Sens. 5, 5702-5724.https://doi.org/10.3390/rs5115702.

[13] Decker, S.G., Martin, J.E., 2005. A local energetics analysis of the life cycle differences between consecutive,explosively deepening, continental cyclones. Mon. Wea. Rev. 133, 295-316.https://doi.org/10.1175/MWR-2860.1.

[14] Dedekind, Z., Engelbrecht, F.A., Van der Merwe, J., 2016. Model simulations of rainfall over southern Africa and its eastern escarpment. Water SA 42, 129-143. DOI: 10.4314/wsa.v42i1.13.

[15] Dyson, L., 2015. A heavy rainfall sounding climatology over Gauteng, South Africa, using self-organising maps. Clim. Dyn. 45, 3051-3065. https://doi.org/10.1007/s00382-015-2523-3.

[16] Engelbrecht, C.J., Landman, W.A., Engelbrecht, F.A., Malherbe, J., 2015. A synoptic decomposition of rainfall over the Cape south coast of South Africa. Clim. Dyn. 44,2589-2607.https://doi.org/10.1007/s00382-014-2230-5.

[17] Fauchereau, N., Pohl, B., Reason, C.J.C., Rouault, M., Richard, Y., 2009. Recurrent daily OLR patterns in the southern Africa/Southwest Indian Ocean region, implications for south African rainfall and teleconnections. Clim. Dyn. 32, 575-591.https://doi.org/10.1007/s00382-008-0426-2.

[18] Favre, A., Hewitson, B., Lennard, C., Cerezo-Mota, R., Tadorss, M., 2013. Cut-off Lows in the South Africa region and their contribution to precipitation. Clim. Dyn. 41, 2331-2351.https://doi.org/10.1007/s00382-012-1579-6

[19] Funatsu, B.M., Waugh, D.W., 2008. Connection between potential vorticity intrusions and convection in the eastern tropical Pacific. J. Atmos. Sci. 65, 987 - 1002.https://doi.org/10.1175/2007JAS2248.1.

[20] Harr, P.A., Dea, J.M., 2009. Downstream development associated with the extratropical transition of tropical cyclones over the western North Pacific. Mon. Wea. Rev. 137, 1295-1319. https://doi.org/10.1175/2008MWR2558.1.

[21] Harrison, M.S.J., 1984. A generalized classification of South African

summer rain-bearing synoptic systems. J. Climatol. 4, 547-560. https://doi.org/10.1002/joc.3370040510.

[22] Hart, N.C.G., Reason, C.J.C., Faucherau, N., 2010. Tropical-extratropical interactions over southern Africa: Three cases of heavy summer season rainfall. Mon. Wea. Rev. 138, 2608-2623.https://doi.org/10.1175/2010MWR3070.1.

[23] Hart, N.C.G., Reason, C.J.C., Fauchereau, N., 2012. Building a tropical extratropical cloud band metbot. Mon. Wea. Rev. 140,4005-4016.https://doi.org/10.1175/MWR-D-12-00127.1.

[24] Hart, N.C.G., Reason, C.J.C., Fauchereau, N., 2013. Cloud bands over southern Africa: seasonality, contribution to rainfall variability and modulation by the MJO. Clim. Dyn. 41,1199-1212. https://doi.org/10.1007/s00382-012-1589-4.

[25] Hersbach, H., Bell, B., Berrisford, P., Hirahara, S., Hor anyi, A., Munoz-Sabater, J., Nicolas, J., Peubey, C., Radu, R., Schepers, D., Simmons, A., Soci, C., Abdalla, S., Abellan, X., Balsamo, G., Bechtold, P., Biavati, G., Bidlot, J., Bonavita, M., De Chiara, G., Dahlgren, P., Dee, D., Diamantakis, M., Dragani, R., Flemming, J., Forbes, R., Fuentes, M., Geer, A., Haimberger, L., Healy, S., Hogan, R.J., Holm, E., Janiskova, M., Keeley, S., Laloyaux, P., Lopez, P., Lupu, C., Radnoti, G., de Rosnay, P., Rozum, I., Vamborg, F., Villaume, S., Thepaut, J.-N., 2020. The ERA5 global reanalysis. Q. J. R. Meteorol. Soc. 146, 1999 - 2049. https://doi.org/10.1002/qj.3803.

[26] Holton, J.R., Hakim, G.J., 2014. An Introduction to Dynamic Meteorology. 4th ed. Elsevier Academic Press, 553 pp. https://doi.org/10.1119/1.1987371.

[27] Hoskins, B.J., Ambrizzi, T., 1993. Rossby wave propagation on a realistic longitudinally varying flow. J. Atmos. Sci. 50, 1661-1671. https://doi.org/10.1175/1520-0469(1993)050¡1661:RWPOAR¿2.0.CO;2.

[28] Hoskins, B.J., McIntyre, M.E, Robertson, A.C., 1985. On the use and significance of isentropic potential vorticity maps. Q. J. R. Meteorol. Soc. 111, 877-946. https://doi.org/10.1002/qj.49711147002

[29] Howard, E., Washington, R., 2018. Characterizing the Synoptic Expression of the Angola Low. J. Climate. 31, 7148-7165. https://doi.org/10.1175/JCLI-D-18-0017.1.

[30] Howard, E., Washington, R., Hodges, K.I., 2019. Tropical lows in Southern Africa: Tracks, rainfall contributions, and the role of ENSO. J. Geophys. Res.: Atmos. 124, 11009-11032. https://doi.org/10.1029/2019JD030803.

[31] Jury, M.R., 2018. Modulation of currents near Durban. Reg. Stud. Mar. Sci. 18, 208-218.https://doi.org/10.1016/j.rsma.2017.10.009.

[32] Keyser, D., Shapiro, M.A, 1986. A review of the structure and dynamics of upper-level frontal zones. Mon. Wea. Rev. 114, 452-499. https://doi.org/10.1175/1520-0493(1986)114¡0452:AROTSA¿2.0.CO;2.

[33] Lackmann, G.M., Keyser, D., Bosart, L.F., 1999. Energetics of an intensifying jet streak during the Experiment on Rapidly Intensifying Cyclones over the Atlantic (ERICA). Mon. Wea. Rev. 127, 2777-2795. https://doi.org/10.1175/1520-0493(1999)127¡2777:EOAIJS¿2.0.CO;2.

[34] Lee, S., Held, I.M., 1993. Baroclinic wave packets in models and observations. J. Atmos. Sci. 50, 1413-1428.https://doi.org/10.1175/1520-0469(1993)050¡1413:BWPIMA¿2.0.CO;2.

[35] Liebmann, B. Kiladis, G.N., Marengo, J.A, Ambrizzi, T., Glick, J.D. 1999. Submonthly convective Variability over South America and the South Atlantic convergence zone. J. Climate. 12, 1877-1891. https://doi.org/10.1175/1520-0442(1999)012¡1877:SCVOSA¿2.0.CO;2.

[36] Loveday, B., Durgadoo, J.V., Reason, C.J.C., Penven, P., Biastoch, A., 2014. Decoupling of the Agulhas Leakage from the Agulhas Current. J. Phys. Oceanogr. 44, 1776-1797.https://doi.org/10.1175/JPO-D-13-093.1.

[37] Lutjeharms, J.R.E., 2006. The Agulhas Current, Springer Berlin Heidelberg, 329 pp.https://doi.org/10.1007/3-540-.

[38] Macron, C., Pohl, B., Richard, Y., 2014. How do tropical temperate troughs form and develop over southern Africa. J. Climate. 27,1633-5199.https://doi.org/10.1175/JCLI-D-13-00175.1.

[39] McLay, J.G., Martin, J.E., 2002. Surface cyclolysis in the North Pacific Ocean. Part III: Composite local energetics of tropospheric-deep cyclone decay associated with rapid surface cyclolysis. Mon. Wea. Rev. 130, 2507-2529.https://doi.org/10.1175/1520-0493(2002)130¡2507:SCITNP¿2.0.CO;2.

[40] Molekwa, S., Engelbrecht, C.J., Rautenbach, C.J.W., 2014. Attributes of cut-off low induced rainfall over the Eastern Cape Province of South Africa. Theor. Appl. Climatol. 118, 307-318.https://doi.org/10.1007/s00704-013-1061-3.

[41] Morgan, M.C., 1999. Using piecewise potential vorticity inversion to diagnose frontogenesis. Part I: A partitioning of the Q vector applied to diagnosing surface frontogenesis and vertical motion. Mon. Wea. Rev. 127, 2796-2821. https://doi.org/10.1175/1520-0493(1999)127¡2796:UPPVIT¿2.0.CO;2.

[42] Munday, C., Washington, R., 2017. Circulation controls on southern African precipitation in coupled models: The role of the Angola Low. J Geophys. Res. Atmos. 122, 861-877.https://doi.org/10.1002/2016JD025736.

[43] Ndarana, T., Bopape, M., Waugh, D., Dyson, L., 2018. The influence of the lower stratosphere on ridging Atlantic Ocean anticyclones over South Africa. J. Climate. 31, 6175-6187. https://doi.org/10.1175/JCLI-D-17-0832.1.

[44] Ndarana, T., Rammopo, T.S., Chikoore, H., Barnes, M.A., Bopape, M., 2020. A quasigeostrophic diagnosis of cut-off low pressure systems over South Africa and surrounding ocean. Clim. Dyn. 55, 2631-2644.https://doi.org/10.1007/s00382-020-05401-4.

[45] Ndarana, T., Mpati, S., Bopape, M., Engelbrecht, F.A., Chikoore, H. 2021a. The flow and moisture fluxes associated with ridging South Atlantic Ocean anticyclones during the subtropical southern African summer. Int. J. Climatol. 41, E1000-E1017. https://doi.org/10.1002/joc.6745.

[46] Ndarana, T., Rammopo, T.S., Bopape, M., Reason, C.J.C., Chikoore, H., 2021b. Downstream development during South African cut-off pressure systems. Atmos. Res. 249,105315.https://doi.org/10.1016/j.atmosres.2020.105315

[47] Ndarana, T., Waugh, D.W. 2010. The link between cut-off lows and Rossby wave breaking in the Southern Hemisphere. Q. J. R. Meteorol. Soc. 136, 869-885. https://doi.org/10.1002/qj.627.

[48] O'Brien, L., Reeder, M.J., 2017. Southern Hemisphere summertime Rossby waves and weather in the Australian region. Q. J. R. Meteorolog. Soc. 143, 2374-2388.https://doi.org/10.1002/qj.3090.

[49] O'Kane, T.J., Risbey, J.S., Monselesan, D.P., Horenko, T. Franzke, C.L.E., 2016. On the dynamics of persistent states and their secular trends in the wave guides of the southern hemisphere troposphere. Clim. Dyn. 46, 3567-3597. https://doi.org/10.1007/s00382-015-2786-8.

[50] Orlanski, I., Katzfey, J., 1991. The life cycle of a cyclone wave in the Southern Hemisphere. 1. Eddy energy budget. J. Atmos. Sci. 48, 1972-1998.https://doi.org/10.1175/1520-0469(1991)048¡1972:TLCOAC¿2.0.CO;2.

[51] Orlanski, I., Sheldon, J., 1993. A case of downstream baroclinic development over western North America. Mon. Wea. Rev. 121, 2929-2950.https://doi.org/10.1175/1520-0493(1993)121¡2929:ACODBD¿2.0.CO;2

[52] Orlanski, I., Sheldon, J., 1995. Stages in the energetics of baroclinic systems. Tellus. 47A, 605-628.https://doi.org/10.1034/j.1600-0870.1995.00108.x.

[53] Rapolaki, R. S., Blamey, R.C., Hermes, J.C., Reason, C.J.C, 2020. Moisture sources associated with heavy rainfall over the Limpopo River basin, southern Africa. Clim. Dyn. 55, 1473-1487. https://doi.org/10.1007/s00382-020-05336-w

[54] Ratna, S.B., Behera, S., Ratnam, J.V., Takahashi, K., Yamagata, T., 2013. An index for tropical temperate troughs over southern Africa. Clim. Dyn. 41,421-441.DOI 10.1007/s00382-012-1540-8

[55] Reason, C.J.C., Jagadheesha, D., 2005. A model investigation of recent ENSO impacts over southern Africa. Meteorol. Atmos. Phys. 89, 181-205. https://doi.org/10.1007/s00703-005-0128-9.

[56] Reason, C.J.C., Mulenga, H.M., 1999. Relationships between South African rainfall and SST anomalies in the South West Indian Ocean. Int. J. Climatol, 19, 1651-1673.https://doi.org/10.1002/(SICI)1097-0088(199912)19:15¡1651::AID-JOC439¿3.0.CO;2-U

[57] Reboita, M.S., da Rocha, R. P., Ambrizzi, T., Sugahar, S., 2010. South Atlantic Ocean cyclogensis climatology simulated by a regional climate model (RegCM3). Clim. Dyn. 35, 1331-1347.DOI 10.1007/s00382-009-0668-7

[58] Reid, K.J., Simmond. I., Vincent C.L., King, A.D. 2019. The Australian Northwest Cloudband: Climatology, Mechanisms, and Association with Precipitation. J. Climate. 32, 6665-6684.https://doi.org/10.1175/JCLI-D-19-0031.1

[59] Rehman, S.U., Khan, K., Simmonds, I., 2019. Links between Tasmanian precipitation variability and the Indian Ocean subtropical high. Theor. Appl. Climatol. 138, 1255-1267.https://doi.org/10.1007/s00704-019-02891-z.

[60] Reyers, M., Shao, Y. 2019. Cutoff lows off the coast of the Atacama Desert under present day conditions and in the Last Glacial Maximum. Global Planet. Change. 181, 102983.https://doi.org/10.1016/j.gloplacha.2019.102983

[61] Rocha, A., Simmonds, I. 1997a. Interannual variability of south-eastern African summer rainfall. Part I. relationships with air-sea interaction processes. Int. J. Climatol. 17, 235-265.https://doi.org/10.1002/(SICI)1097-0088(19970315)17:3¡235::AID-JOC123¿3.0.CO;2-N

[62] Rocha, A., Simmonds, I. 1997b. Interannual variability of south-eastern African summer rainfall. Part II. Modelling the impact of sea-surface temperatures on rainfall and circulation. Int. J. Climatol. 17, 267 - 290.https://doi.org/10.1002/(SICI)1097-0088(19970315)17:3¡267::AID-JOC124¿3.0.CO;2-B.

[63] Roffe, S.J., Fitchett, J.M., Curtis, C.J., 2019. Classifying and mapping rainfall seasonality in South Africa: a review. S. Afr. Geog. J., 101(2), 158-174.https://doi.org/10.1080/03736245.2019.1573151.

[64] Røsting, B., Kristjánsson, J.E., 2012. The usefulness of piecewise potential vorticity inversion. J. Atmos. Sci. 69, 934-941. https://doi.org/10.1175/JAS-D-11-0115.1.

[65] Simmonds, I., Keay, K., Lim E-P, 2003. Synoptic activity in the seas around Antarctica. Mon. Wea. Rev. 131, 272 - 288. https://doi.org/10.1175/1520-0493(2003)131¡0272:SAITSA¿2.0.CO;2.

[66] Simmonds, I., Li, M. 2021. Trends and variability in polar sea ice, global atmospheric circulations and baroclinicity. Ann. NY Acad. Sci. https://doi.org/10.1111/nyas.14673.

[67] Singleton, A.T., Reason, C.J.C., 2006. Numerical simulations of a severe rainfall event over the Eastern Cape coast of South Africa: sensitivity to sea surface temperature and topography. Tellus A: Dyn. Meteorol. Oceanogr. 58(3), 335-367.https://doi.org/10.1111/j.1600-0870.2006.00180.x.

[68] Singleton, A.T. and C.J.C. Reason, 2007a: Variability in the characteristics of cut-off low pressure systems over subtropical southern Africa. Int. J. Climatol., 27, 295-310.https://doi.org/10.1002/joc.1399

[69] Singleton, A.T., Reason, C.J.C., 2007b. A numerical study of an intense cut-off low pressure system over South Africa. Mon. Wea. Rev. 135, 1128-1150.https://doi.org/10.1175/MWR3311.1

[70] Sun, X., Cook, K.H., Vizy, E.K., 2017. The South Atlantic subtropical high: Climatology and interannual variability, J. Climate. 30, 3279 - 3296.https://doi.org/10.1175/JCLI-D-16-0705.1.

[71] Stander, J.H., Dyson, L., Engelbrecht, C.J., 2016. A snow forecasting decision

tree for significant snowfall over the interior of South Africa. S. Afr. J. Sci. 112, 29-38.http://dx.doi.org/10.17159/sajs.2016/20150221.

[72] Taljaard, J.J., 1985. Cut-off lows in the South African region. South African Weather Bureau Tech. Paper 14, 153.[Available from the South African Weather Service, Private Bag x097, Pretoria, 0001, South Africa.]

[73] Todd, M.C., Washington, R., Palmer, P.I., 2004. Water vapour transport associated with tropical temperate trough systems over southern Africa and the southwest Indian Ocean. Int. J. Climatol. 24, 555-568. https://doi.org/10.1002/joc.1023

[74] Trigaardt, D.O., Terblanche, D.E., van Heerden, J., Laing, M.V., 1988. The Natal flood of September 1987. South African Weather Bureau Tech. Paper 19, 62 pp. [Available from the South African Weather Service, Private Bag x097, Pretoria, 0001, South Africa.]

[75] Tyson, P.D., Preston-Whyte, R.A., 2000. The Weather and Climate of Southern Africa. Oxford University Press, 396 pp.

[76] Uccellini, L.W., Kocin, P.J., 1987. The interaction of jet streak circulations during heavy snow events along the east coast of the United States. Weather. Forecasting. 2, 289-308. https://doi.org/10.1175/1520-0434(1987)002¡0289:TIOJSC¿2.0.CO;2.

[77] van Heerden, J., Taljaard, J.J., 1998. Africa and surrounding waters. Meteorology of the Southern Hemisphere. Meteor. Monogr. No. 49, Amer. Meteor. Soc., 141-174.

[78] Vigaud, N., Richard, Y., Rouault, M., Fauchereau, N., 2007. Water vapour transport from the tropical Atlantic and summer rainfall in tropical southern Africa. Clim. Dyn. 28,113-123. DOI 10.1007/s00382-006-0186-9.

[79] Wang, C.-H., Lin, K.-Y., Davis, C.A., Huang, S.-U., Liu, C.-S., Tsuboki, K., Jou, B.J.-D., 2020. A Modeling Study on the Impacts of Typhoon Morakot

(2009)s Vortex Structure on Rainfall in Taiwan through the Use of Piecewise Potential Vorticity Inversion. J. Meteorolog. Soc. Jpn. 136, 869-885. https://doi.org/10.2151/jmsj.2020-036.

[80] Waugh, D.W., Funatsu, B.M., 2003. Intrusions into the tropical upper troposphere: Three-dimensional structure and accompanying ozone and OLR distributions. J. Atmos. Sci. 60, 637-653.https://doi.org/10.1175/1520-0469(2003)060¡0637:IITTUT¿2.0.CO;2.

[81] Webster, E.M., 2018. A synoptic climatology of continental tropical low pressure systems over southern Africa and their contribution to rainfall over South Africa. Unpublished M.Sc. Dissertation, University of Pretoria. pp 96.

[82] Weldon, D., Reason, C.J.C., 2014. Variability of rainfall characteristics over the South Coast region of South Africa. Theor. Appl. Climatol. 115, 177-185. https://doi.org/10.1007/s00704-013-0882-4.

[83] Xue, M,, Luo, X., Zhu, K., Sun, Z., Fei, J., 2018. The controlling role of boundary layer inertial oscillations in Meiyu frontal precipitation and its diurnal cycles over China. J. Geophy. Res. Atmos. 123, 5090-5115. https://doi.org/10.1029/2018JD028368.

[84] Xulu, N.G., Chikoore, H., Bopape, M.M., Nethengwe, N.S., 2020. Climatology of the Mascarene High and its influence on weather and climate over Southern Africa. Climate. 8, 86.https://doi.org/10.3390/cli8070086

[85] Zilli, M.T., Hart, N.C.G. 2021. Rossby Wave dynamics over South America explored with automatic tropicalextratropical cloud band identification framework. J. Climate. 34, 81258144.https://doi.org/10.1175/JCLI-D-21-0020.1.

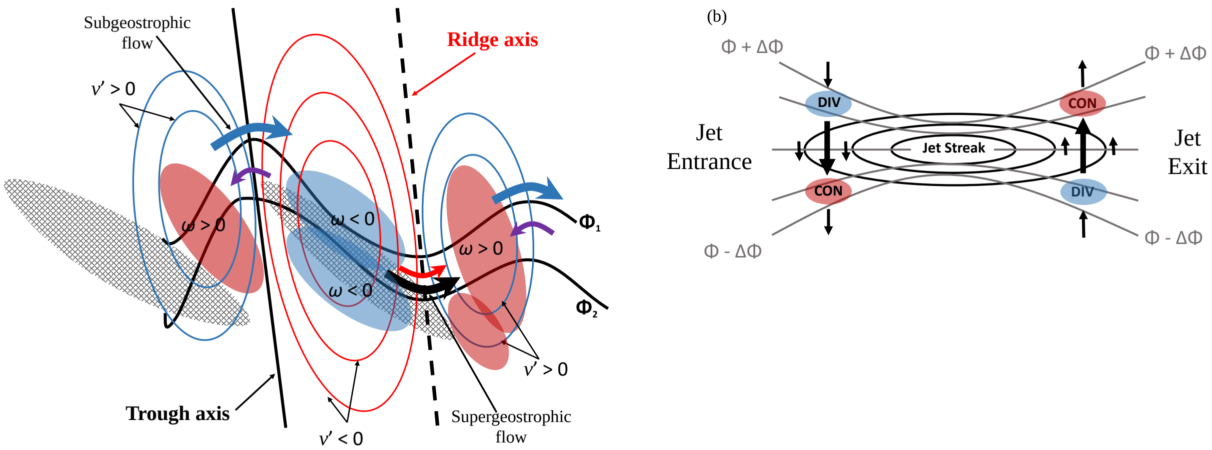

Figure 1: (a) Schematic of geopotential contours (black contours) representing a trough/ridge system in the Southern Hemisphere with the perturbation meridional velocity field $v' > 0$ and $v' < 0$. The thick black solid (dashed) straight is the trough (ridge) axis. The area shaded in red (blue) at the inflection points of the wave represents downward (upward) vertical motion. The thick blue curved arrows represent the subgeostrophic flow, with the associated ageostrophic flow represented by the curved purple arrow. The supergeostrophic flow across the ridge axis is presented by the thick black curved arrow and the associated ageostrophic flow is represented by the red arrow. The hatched structures represent the upstream and downstream jet streaks. (b) Schematic representation of ageostrophic motions (arrows) and associated patterns of convergence (CON) and divergence (DIV) in a straight jet streak in the absence of along-contour thermal advection. The shading of CON and DIV centres at the jet entrance and exit are presented in a way that is consistent to the vertical motions in Fig. 1(a). [Adapted from Keyser and Shapiro (1986); Uccellini and Kocin (1987); Orlanski and Sheldon (1995); Ndarana and Waugh (2010); Reyers and Shao (2019); Ndarana et al. (2020); Ndarana et al. (2021b)].

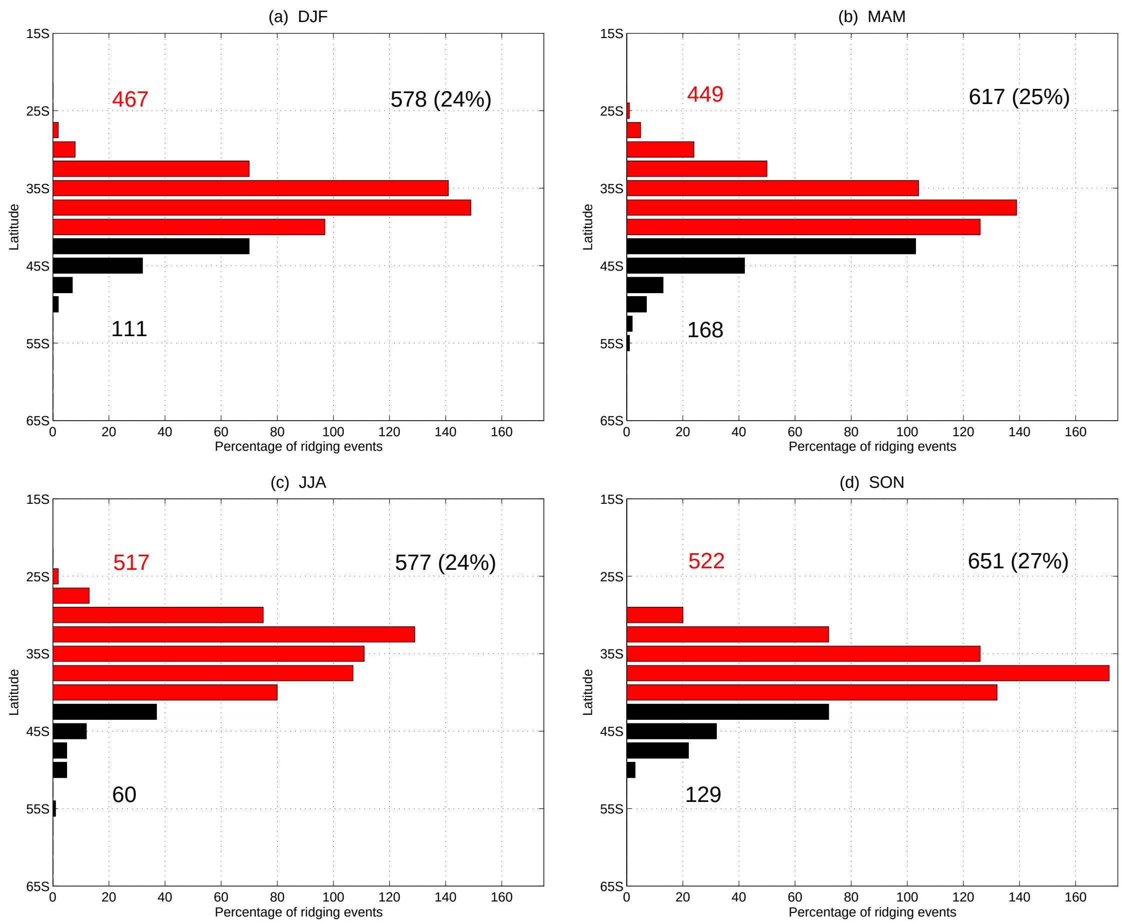

Figure 2: The frequency of occurrence of ridging South Atlantic Ocean high pressure systems as a function of latitude for (a) DJF, (b) MAM, (c) JJA and (d) SON. Events that occur north of 40°S are represented by the red histograms, the black bars represents the frequency of events occurring south of this latitude line and their respective total frequencies are indicated in the same color as the histograms. The number of events (and percentage given in brackets) per season with respect to the total number of events is shown in the top right corner of each panel.

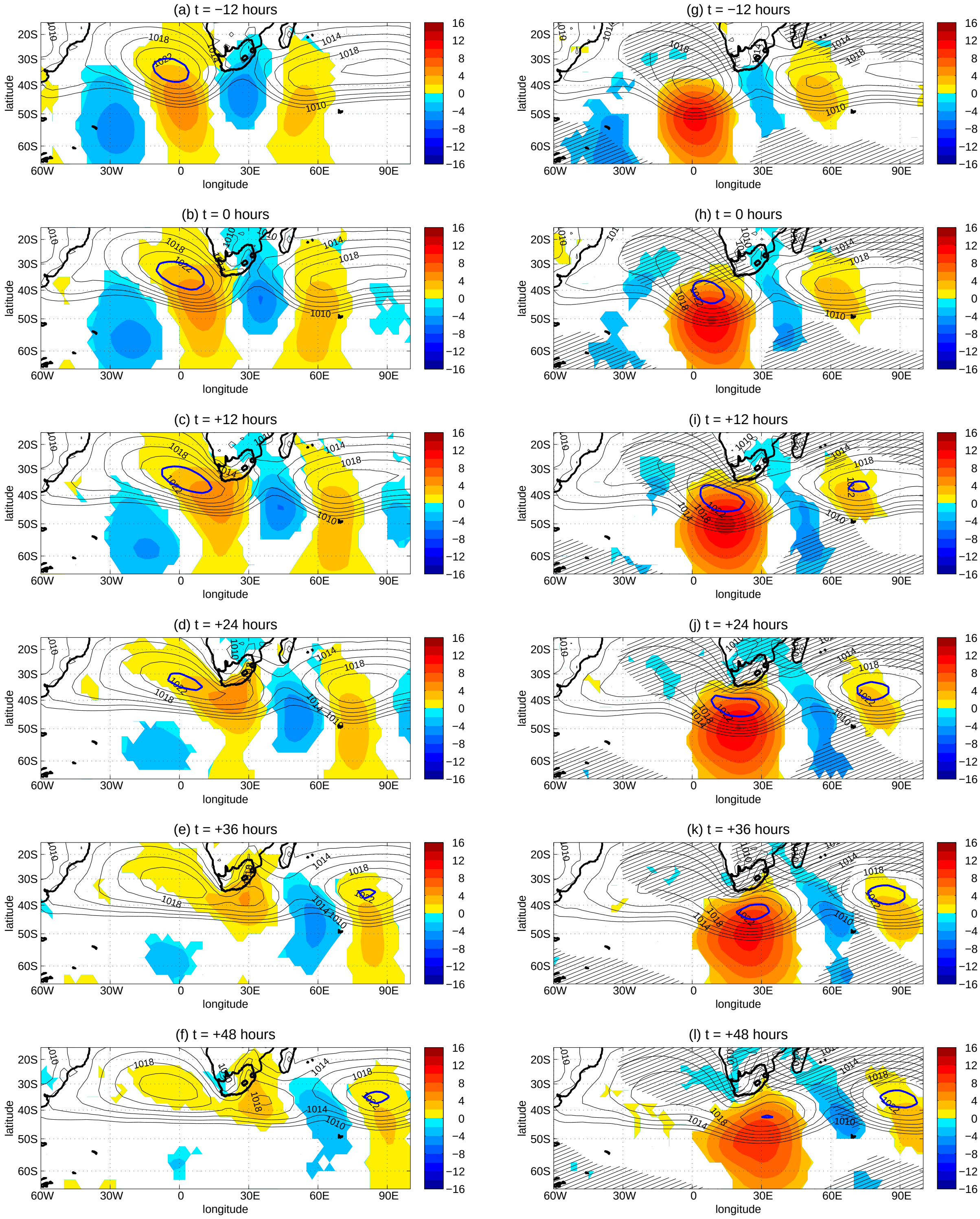

Figure 3: Time-lagged composite evolution of mean sea level pressure (MSLP) represented by the thin black contours for Type-N (left panels) and Type-S (right panels) ridging events for DJ. The MSLP isobars are plotted at 2 hPa contour intervals. The thick blue contour represents the 1022 hPa MSLP isobar. The shaded region are the MSLP perturbation fields that are induced by the ridging process. Only the anomalies significant at the 95% level are shown. The hatched regions on the right panels indicates where the difference Δ MSLP = MSLP (Type-N) - MSLP (Type-S) is positive indicating where stronger MSLP values associated with Type-N events are larger. The composite are plotted in 12 hour intervals from (a,g) t = -12 hours to (f,l) t = +48 hours.

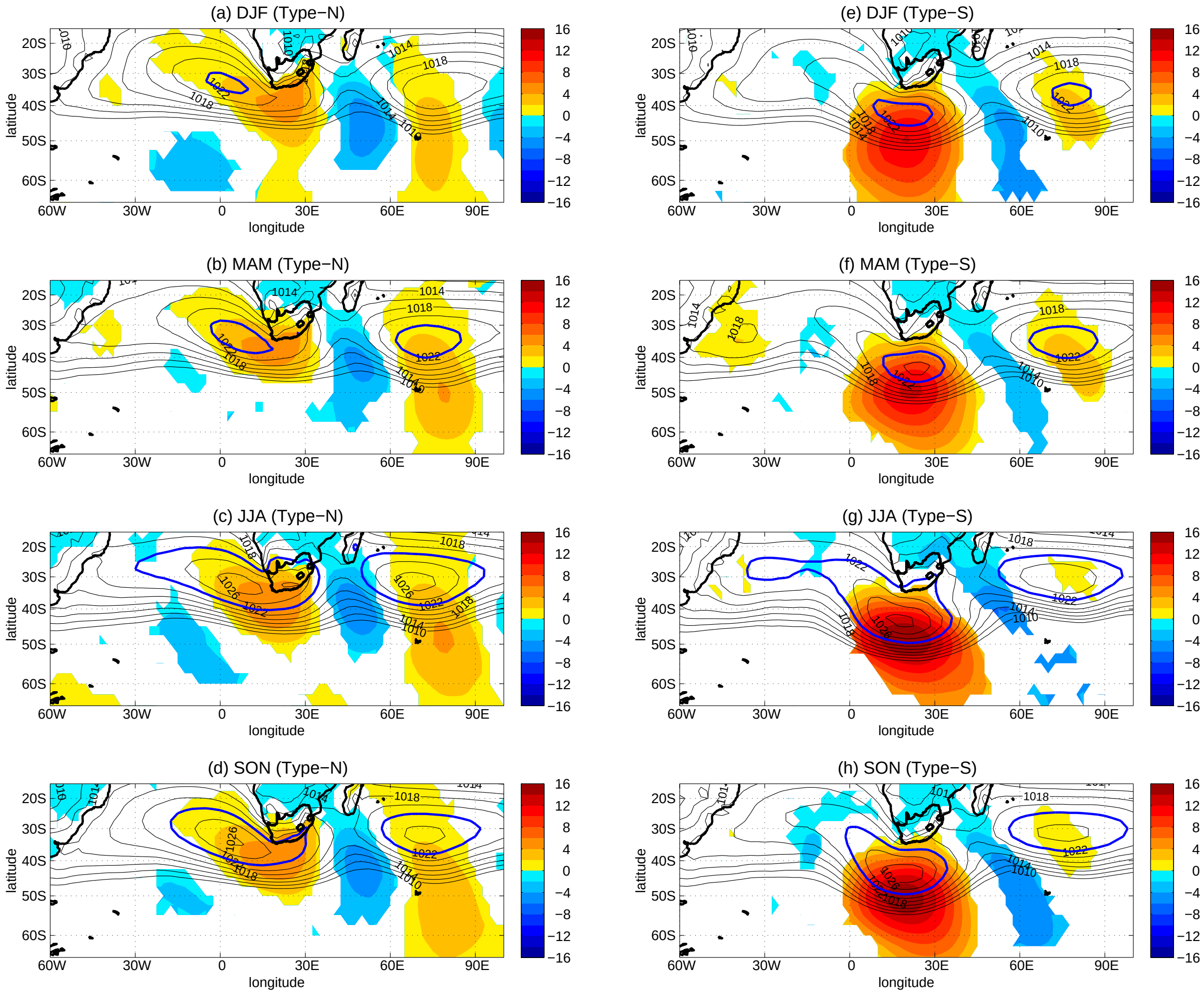

Figure 4: Same as in Fig. 3 but only for t = +24 hours for (a,e) DJF, (b,f) MAM, (c,g) JJA and (d,h) SON.

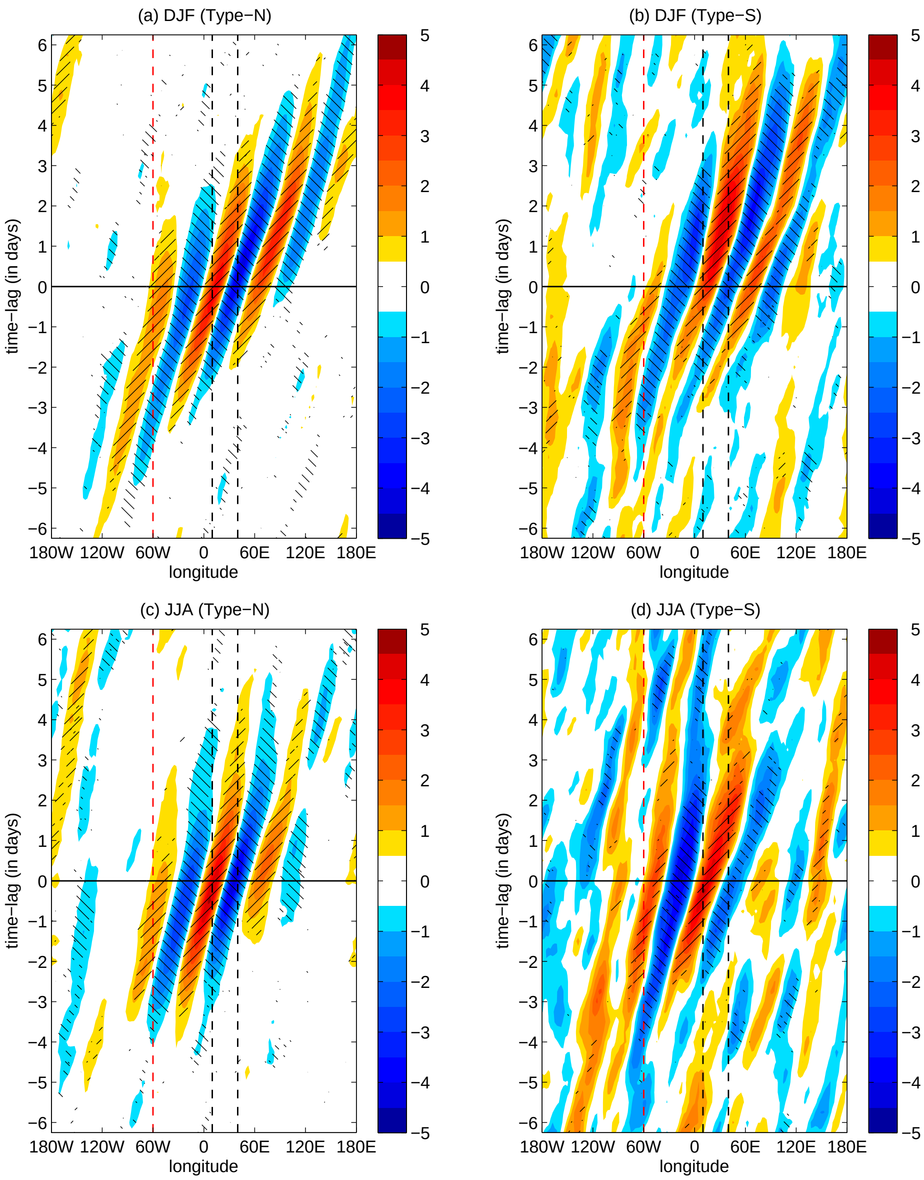

Figure 5: Hovmöller plot of composite mean 250 hPa v' field averaged between 60°S and 35°S for Type-N (left panels) and Type-S (right panels) ridging events for DJF (top panels) and JJA (bottom panels). Only values exceeding 0.5 m s^{-1} are shown. The dotted red line indicates the location of 60°W and the dotted black lines indicate the western (10°E) and eastern (50°E) boundaries of the South African domain. The hatched regions show statistical significance at the 95% level

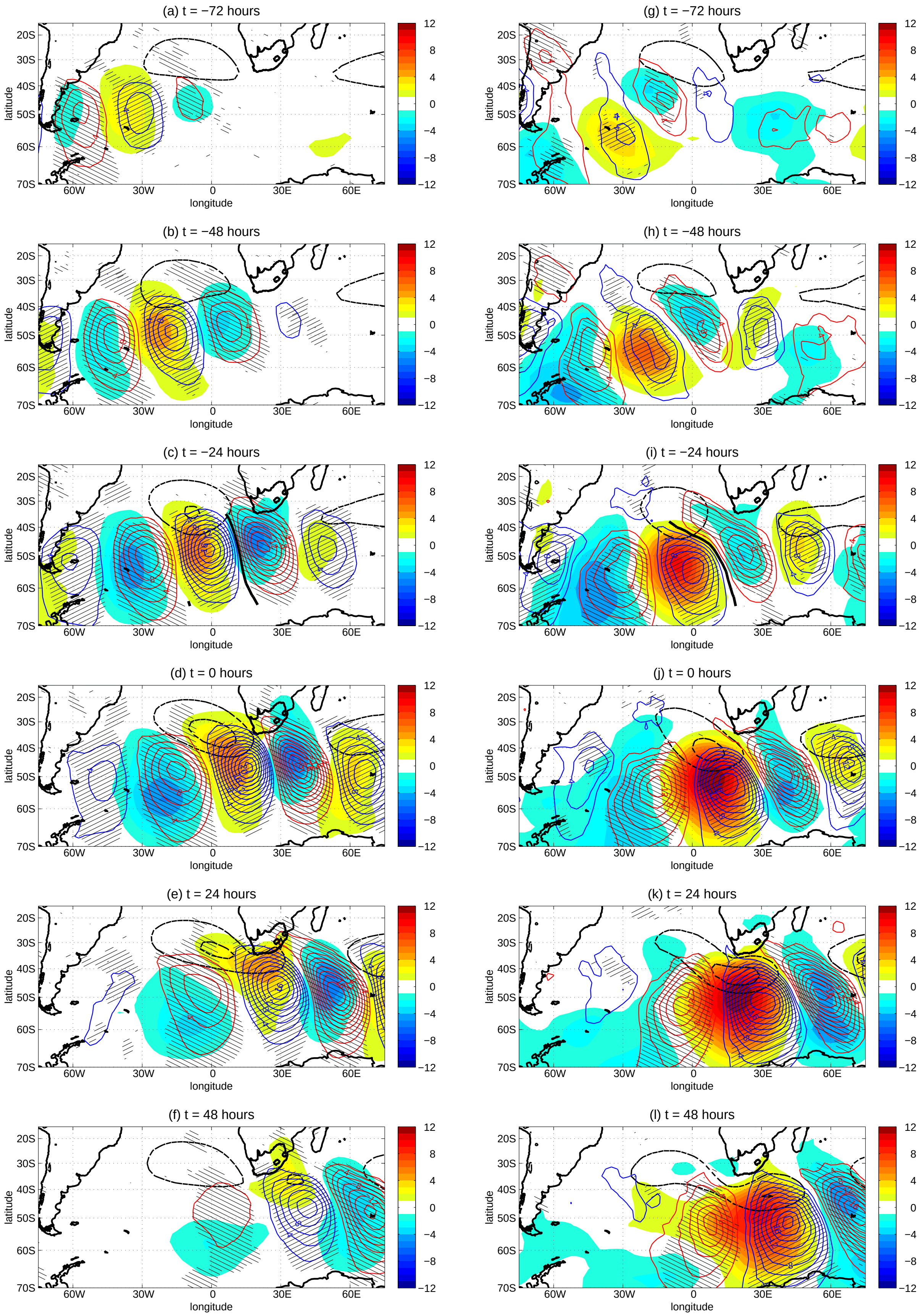

Figure 6: Time-lagged composite evolution of 250 hPa perturbation meridional velocity (v') where thin blue (red) contours represent regions of $v' > 0$ ($v' < 0$) plotted in +2 (-2) m s−1 contour intervals. The hatched regions show where the v perturbation fields are significant at the 95% statistical significant level. The shading represent the MSLP perturbation fields and the thick dashed black contours represent the 1018 and 1022 hPa MSLP contours for Type-N (left panels) and Type-S (right panels) ridging events. The thick solid black contour in panels (c) and (j) represents the main trough axis. The composite are plotted from (a,g) t = -72 hours to (f,l) t = +48 hours.

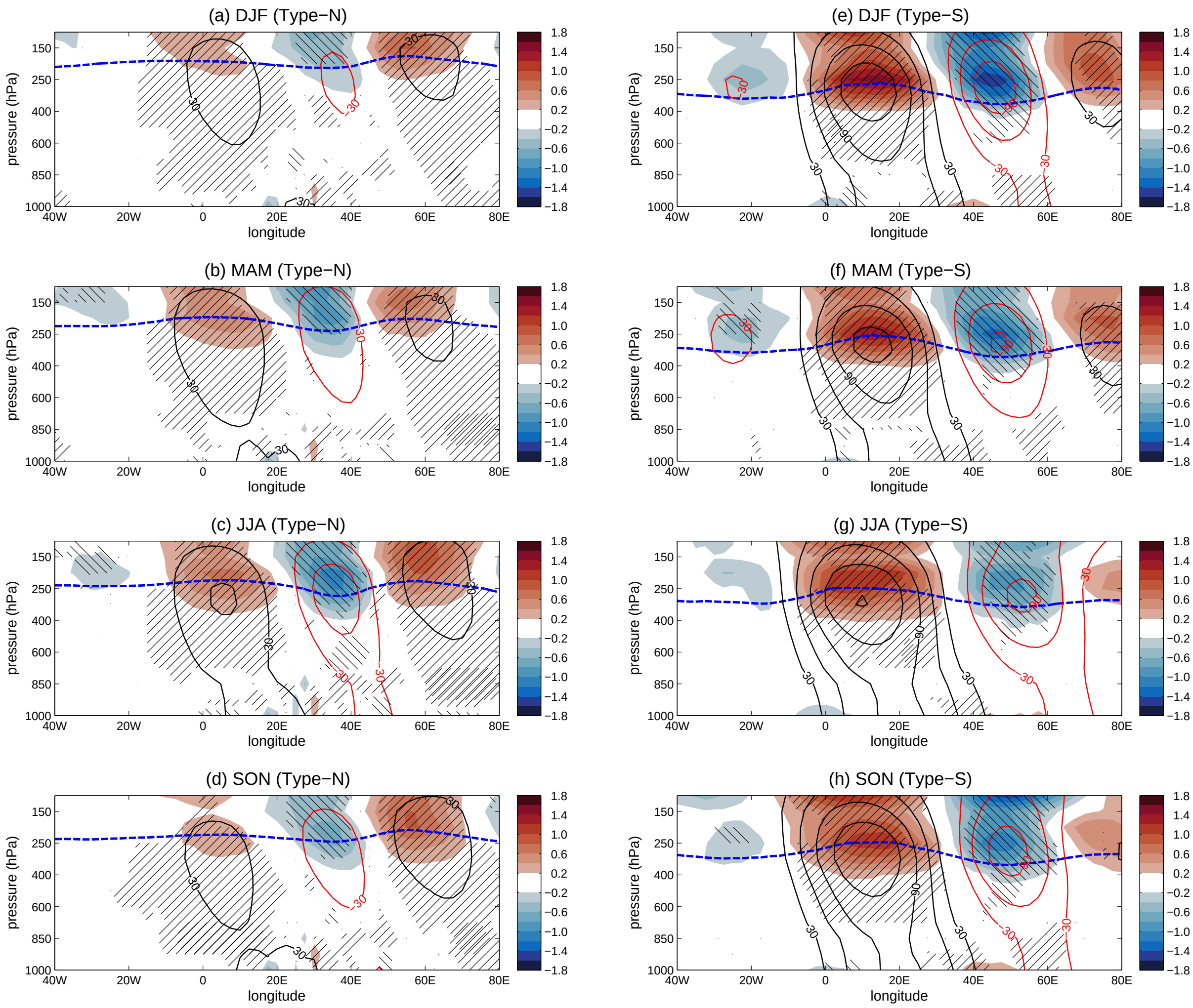

Figure 7: Time-lagged composite of longitudinal vertical profiles at t = +24 hours. The fields shown are potential vorticity anomalies (shaded and plotted in PVU, 1 PVU = 10^6 K m^2 s^{-2} kg^{-1}) and geopotential height anomalies (thin blue and black contours plotted in 30 gpm contour intervals) for Type-N (left panels) and Type-S (right panels) ridging events for (a,e) DJF, (b,f) MAM, (c,g) JJA and (d,h) SON. The fields in the left and right panels were produced by taking the meridional average from 50°S to 40°S, and from 70S and 50S, respectively. The thick dashed blue contour represents the dynamical tropopause (PV = -2 PVU). The composite are plotted from (a,g) t = -12 hours to (f,l) t = +48 hours. The hatched regions represent areas where the potential vorticity and geopotential vorticity anomaly fields are simultaneously significant at the 95% level.

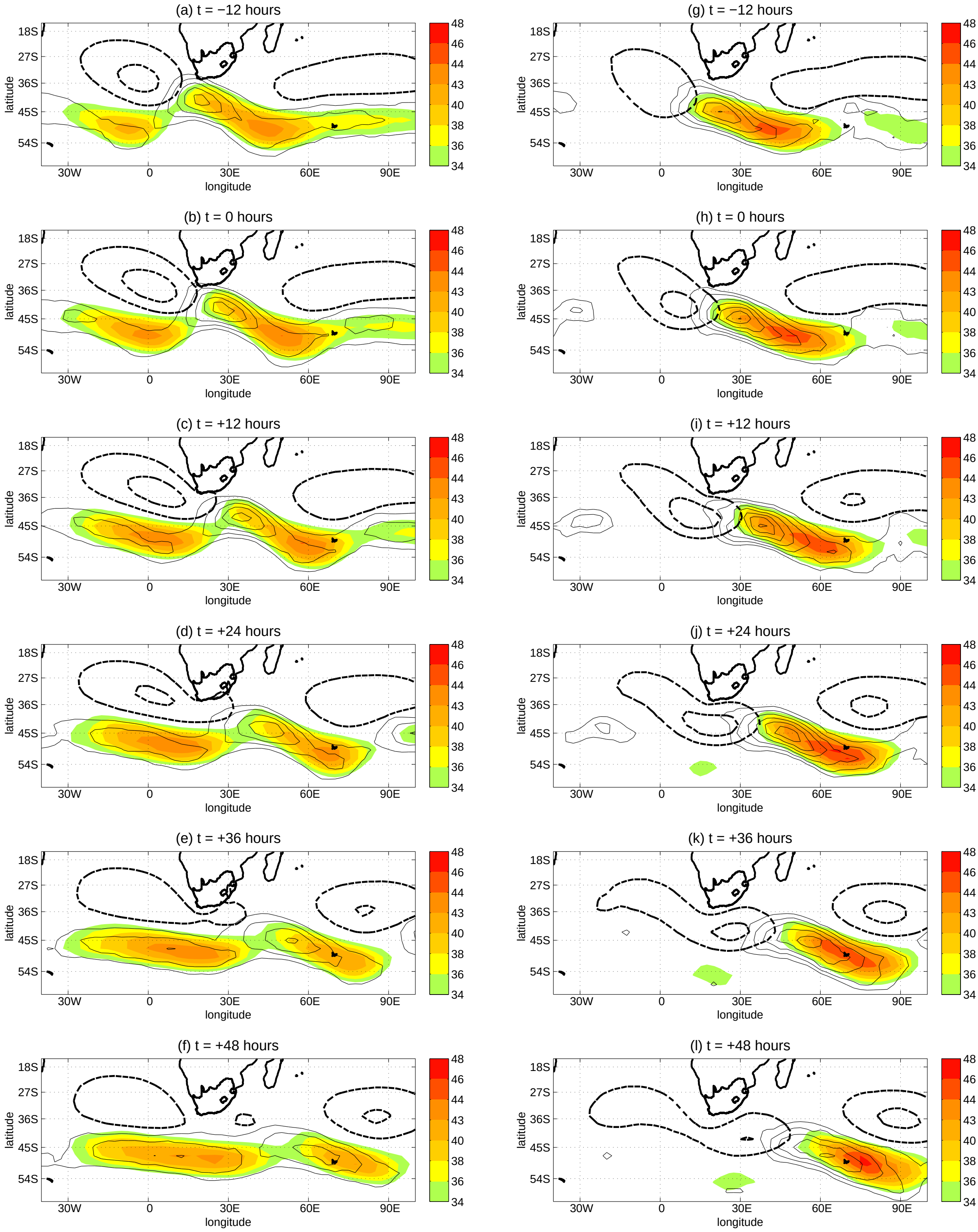

Figure 8: Time-lagged composite evolution of the 250 hPa level zonal wind component (shading) and meridional temperature gradient ($\partial_y T$) represented by the thin black contours, plotted in 1×10^6 K m^{-1} contour intervals. The evolution of the ridging is highlighted by means of the 1018 and 1022 hPa MSLP (thick dashed black) contours. The composite are plotted in 12 hour intervals from (a,g) t = -12 hours to (f,l) t = +48 hours.

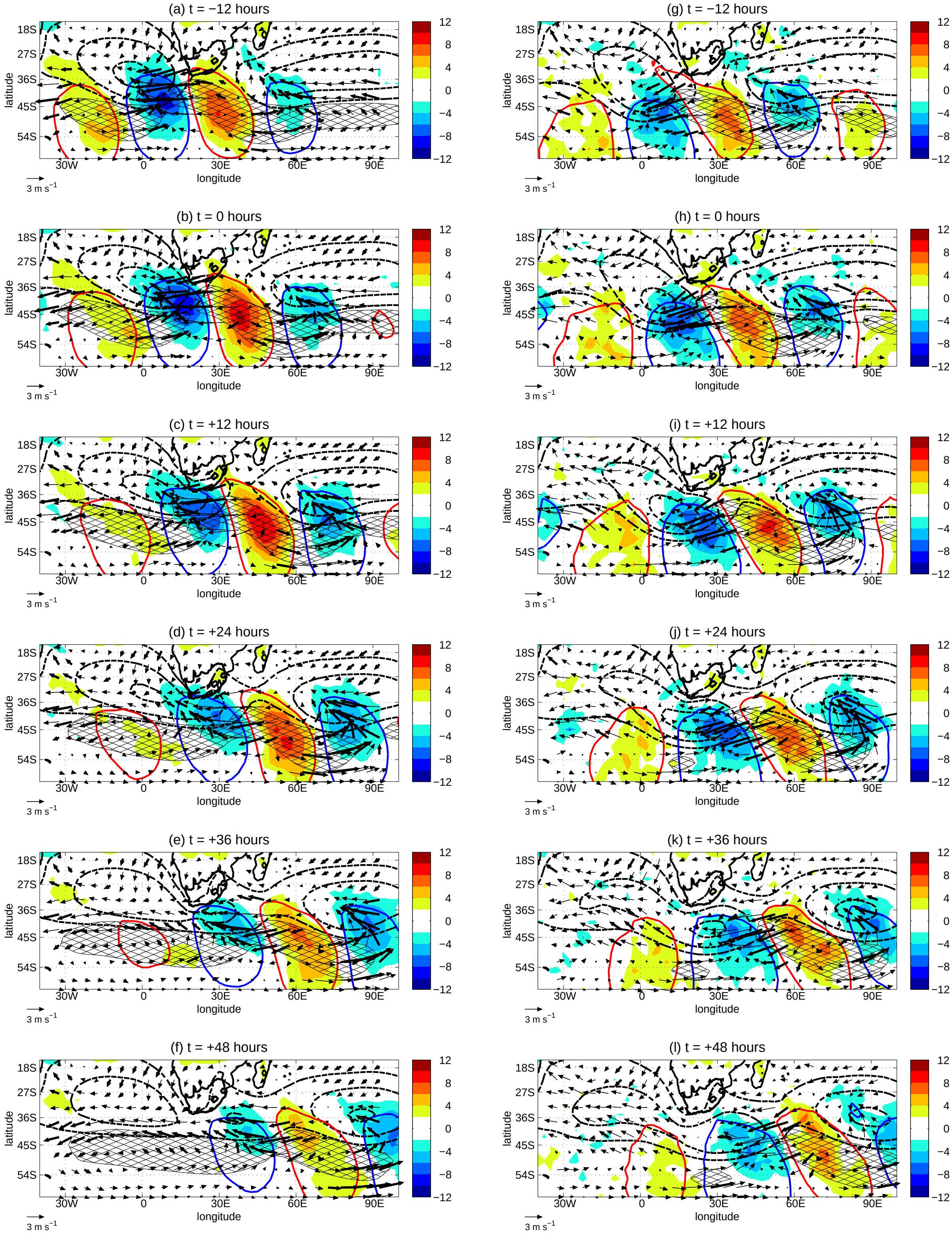

Figure 9: Time-lagged composite evolution of ageostrophic flow (black arrows) and divergence (shaded) at 250 hPa associated with Type-N (left panels) and Type-S (right panels) ridging highs for DJF. The black arrows represent the 250 hPa ageostrophic flow, $\mathbf{u}_a$, with the thicker arrows showing where the flow is statistically significant at the 95% level. The hatched areas are the areas of 250 hPa zonal flow (u) isotachs that exceed 34 m s^{-1}. The solid red and blue contours represent the $v' = -4$ m s^{-1} and $v' = +4$ m s^{-1} isotachs, respectively.The black dashed contours represent the 1018 and 1022 hPa MSLP isobars. The composite are plotted from (a,g) t = -12 hours to (f,l) t = +48 hours.

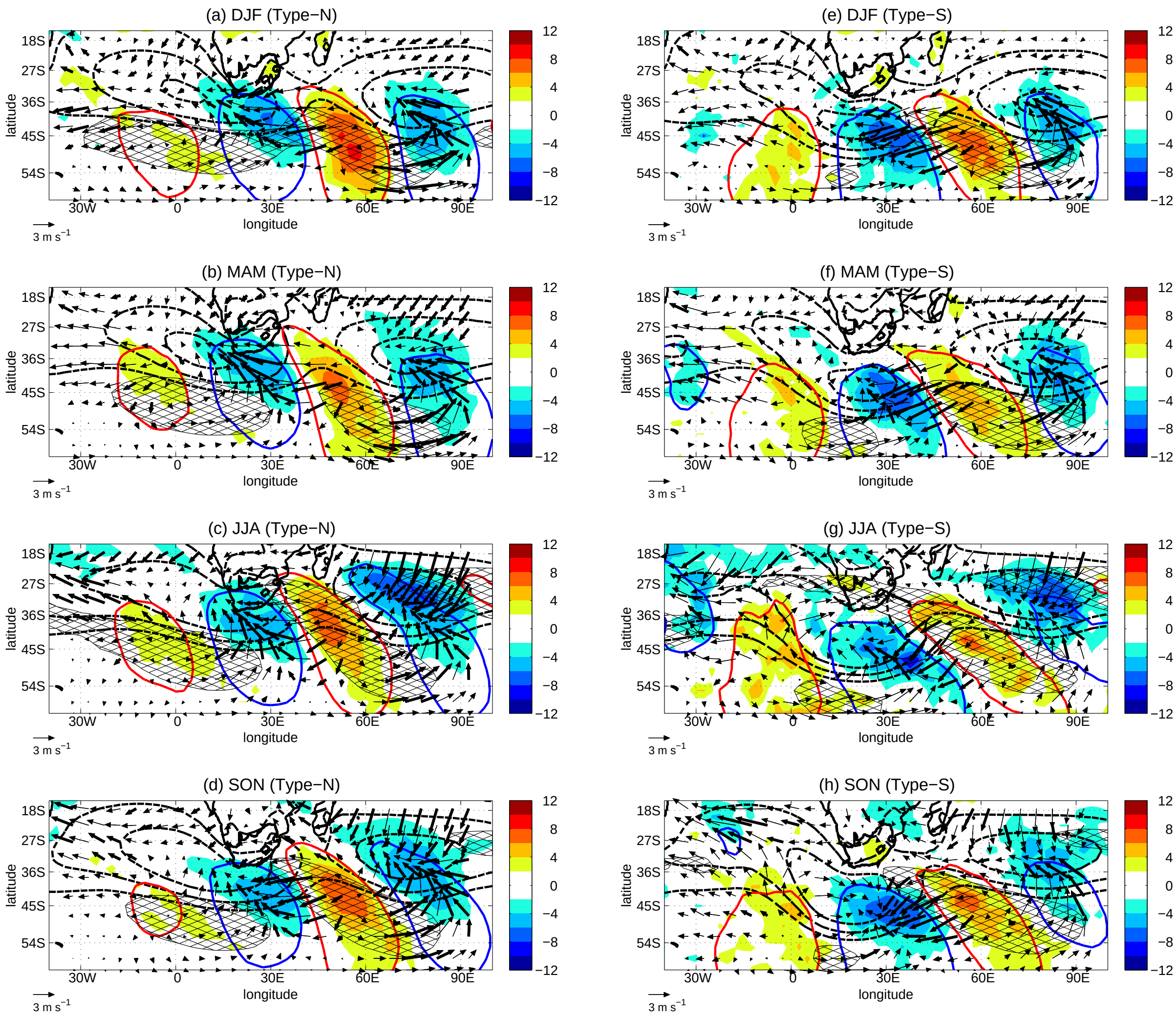

Figure 10: Same as in Fig. 9 but only for t = +24 hours for (a,e) DJF, (b,f) MAM, (c,g) JJA and (d,h) SON.

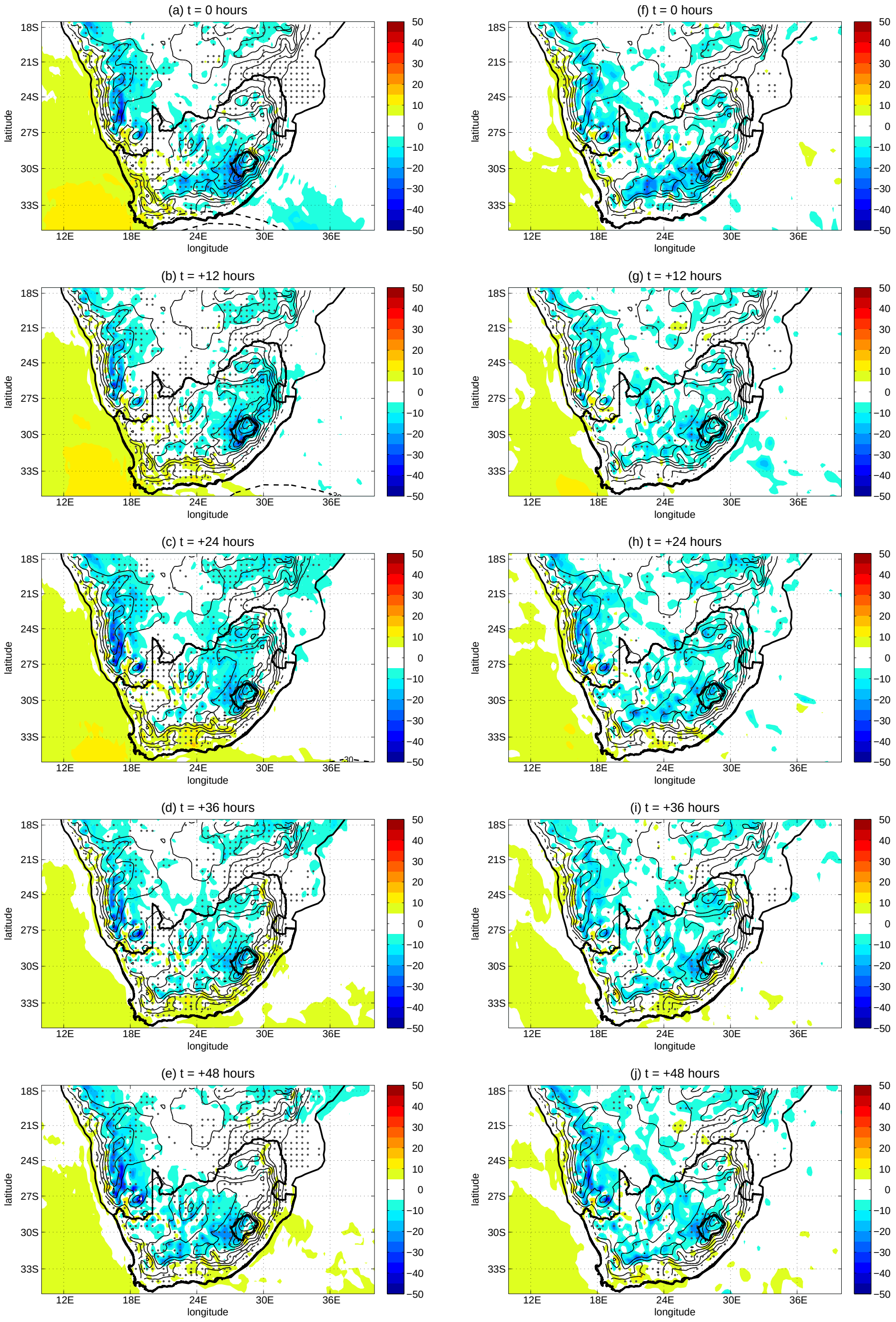

Figure 11: Time-lagged composite evolution of cross-sections of vertical motion (ω) (shaded) and zonal isotachs (dashed black contours) plotted from 30 m s^{-1} in 2 m s^{-1} contour intervals, to high light the position of the jet streak entrance relative to the South African mainland. The dots represent areas where the composite mean of vertical motion is statistically significant at the 95% level. The black contours represent the topography over the southern African interior. The composite are plotted in 12 hour intervals from (a,e) t = 0 hours to (f,j) t = +48 hours.

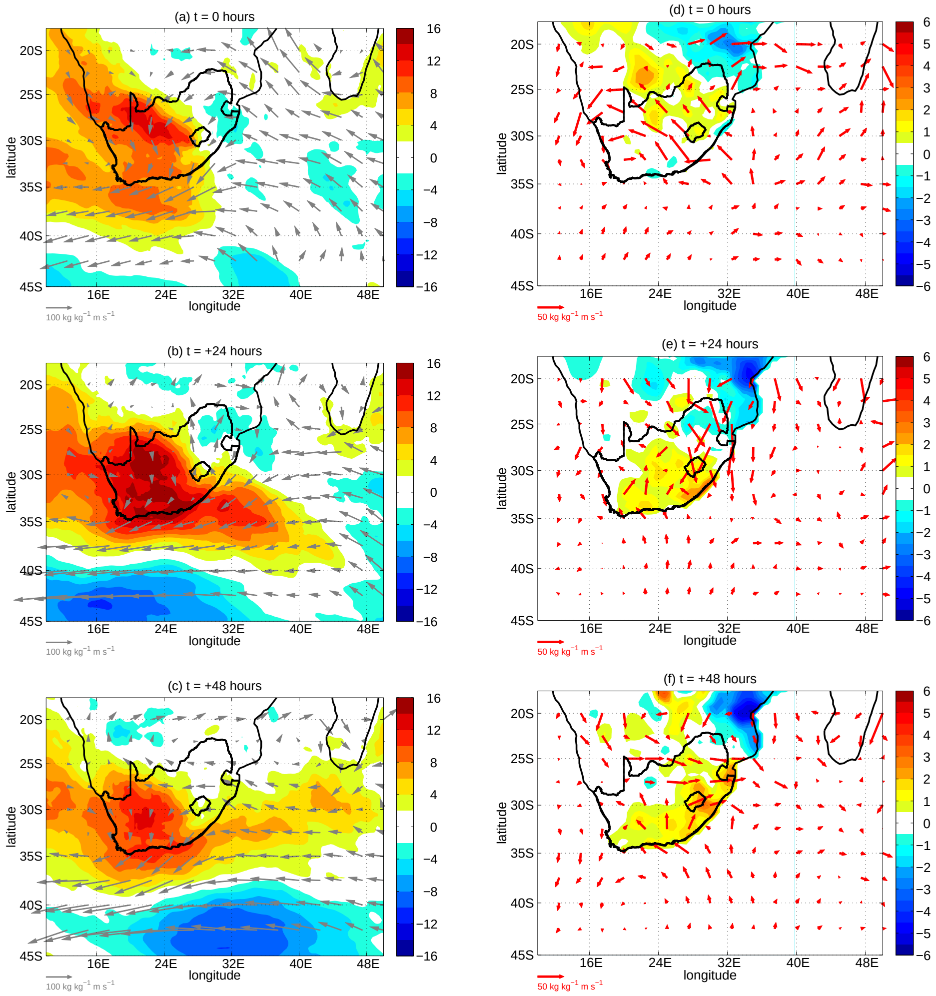

Figure 12: Time-lagged composite evolution of difference in precipitable water ΔPW = PW(Type-S) - PW(Type-N) (shaded) and difference in geostrophic fluxes $\Delta\mathbf{Q}_q = \mathbf{Q}_q$(Type-S) - $\mathbf{Q}_q$(Type-N) (grey arrows) presented in the left panels and the shaded regions in the right panels represented where precipitation ΔP = P(Type-S) - P(Type-N) and the red arrows represent difference in ageostrophic fluxes $\Delta\mathbf{Q}_a = \mathbf{Q}_a$(Type-S) - $\mathbf{Q}_a$(Type-N) is positive (orange-red) and negative (blue). The composite are plotted in 24 hour intervals from (a,d) t = 0 hours to (c,f) t = +48 hours for DJF.